https://doi.org/10.5194/acp-2021-154
Preprint. Discussion started: 23 April 2021
© Author(s) 2021. CC BY 4.0 License.

Atmospheric Chemistry and Physics Discussions

Impacts of tropical cyclones on the thermodynamic conditions in the tropical tropopause layer observed by A-train satellites

Jing Feng[1] and Yi Huang[1]

[1]Department of Atmospheric and Oceanic Sciences, McGill University, Montreal, Canada

Correspondence: Jing Feng (jing.feng3@mail.mcgill.ca)

Abstract.

The tropical tropopause layer (TTL) is the transition layer between the troposphere and the stratosphere. Tropical cyclones may impact the TTL by perturbing the vertical distributions of cloud, temperature, and water vapor, although this impact is poorly quantified due to the lack of collocated data. To address this problem, we implement a synergistic retrieval approach to obtain the thermodynamic profiles and ice water content above thick high-level clouds using the A-Train satellite measurements that pass over the tropical cyclones.

This study detects the signature of cyclone impact on the distribution patterns of cloud, water vapor, temperature, and radiation by compositing these thermodynamic fields with respect to cyclone center locations. It is found that tropical cyclone events considerably increase the occurrence of TTL clouds, in the form of cirrus clouds above a clear troposphere. The amount of TTL cloud ice, however, is found to be mostly contributed by overshooting deep convections that penetrate the bottom of TTL.

Using the synergistic retrieval method, we find a vertically oscillating pattern of temperature anomalies above tropical cyclones, with warming beneath the cloud top (around 16 km) and cooling above. The atmospheric column above 16 km is generally hydrated by overshooting convections, although dehydration is detected above non-overshooting TTL clouds. Above overshooting deep convections, the column-integrated water vapor is found to be on average 40 % higher than the climatology.

Moreover, the TTL is cooled due to longwave radiative cooling above tropical cyclones. The radiative heating rates above cyclones are well differentiated by the brightness temperature of a satellite infrared channel in the window band. Using radiative calculations, it is found that TTL hydration is usually associated with radiative cooling of the TTL, which inhibits the diabatic ascent of moist air. The radiative balance of the TTL under the impact of the cyclone, therefore, is not in favor of maintaining the moist anomalies in the TTL or transporting water vertically to the stratosphere.

1 Introduction

The tropical tropopause layer (TTL, located around 15-18 km) is the transition layer between the convective overturning circulation in the troposphere and the Brewer-Dobson circulation in the stratosphere. Once entering the TTL, air tends to rise into the stratosphere, driven by the positive clear-sky radiative heating rate above the bottom of the TTL, which is marked by the level of zero radiative heating (LZRH).

https://doi.org/10.5194/acp-2021-154
Preprint. Discussion started: 23 April 2021
© Author(s) 2021. CC BY 4.0 License.

The TTL plays an important role in the stratosphere-troposphere exchange (Holton et al., 1995). For example, the cold air at the TTL acts as a 'cold trap' that modulates both the vertical and isentropic (horizontal) transport of water vapor to the lower stratosphere (Dessler et al., 1995; Brewer, 1949; Holton and Gettelman, 2001; Gettelman et al., 2002), where water vapor, despite its low concentration, may have a large impact on radiation, climate, and atmospheric chemistry (Solomon et al., 2010; Anderson et al., 2012; Dessler et al., 2013; Huang et al., 2016).

Given their vertical extent, deep convections potentially provide an important pathway to transport water vapor and other constituents to the stratosphere via the TTL. Deep convections may affect the TTL in several ways. First, tropical deep convections, especially the tropical cyclones, are associated with strong dynamical cooling around the tropopause level (Holloway and Neelin, 2007). Second, the injected ice and water vapor, together with the temperature anomalies caused by deep convection, can modify the radiative heating in the TTL, which in turn can either speed up or slow down the upwelling motion of air and the transport to the stratosphere. Consequently, the air convectively injected into the TTL can be either a source or a sink of water vapor, depending on the pre-existing relative humidity (Jensen et al., 2007; Ueyama et al., 2018; Schoeberl et al., 2018). Simulations and observations have shown that deep convections may hydrate the upper-troposphere and lower-stratosphere (UTLS) by directly injecting water vapor and ice above mid-latitude (Anderson et al., 2012; Sun and Huang, 2015; Qu et al., 2020) and tropical storms (Avery et al., 2017; Schoeberl et al., 2018), or dehydrate it by condensing the pre-existing water vapor to ice particles in a supersaturated environment(Ueyama et al., 2018).

On the other hand, climate models and global reanalysis datasets are subject to common problems in representing the key processes, such as convective parameterization, (e.g., Takahashi et al., 2016), in the UTLS region. These problems include a persistent wet bias in upper tropospheric humidity (Huang et al., 2007; Jiang et al., 2012, 2015), discrepancies in the transportation speed of water vapor from the upper troposphere to the lower stratosphere (Jiang et al., 2015) and the contradictory assessments of diabatic heating under the impact of high clouds in the TTL region (Wright and Fueglistaler, 2013; Wright et al., 2020).

Existing satellite datasets (Waters et al., 2006; Bernath et al., 2005; Anthes et al., 2008) and aircraft campaigns (e.g., Jensen et al., 2013; Lee et al., 2019) have advanced the understanding of the TTL region, although the study of deep convective impacts on the temperature, water vapor, and clouds in the TTL region is still impeded by a lack of collocated measurements of these variables. The A-Train constellation (L'Ecuyer and Jiang, 2011), including Aqua, CloudSat, CALIPSO, PARASOL, and Aura, carries over 20 instruments that monitor clouds and other atmospheric variables. However, the sounding of thermodynamic conditions above deep convection, especially near the convective core, remains a challenge (Livesey et al., 2017; Olsen et al., 2013). Feng and Huang (2018) found that the retrievability of temperature and water vapor is improved by an underlying cloud layer because the cloud layer reduces the degeneracy caused by non-monotonic temperature variation and the smearing effect of lower-level water vapor, and proposed a cloud-assisted retrieval algorithm that can be applied to the infrared hyperspectral measurements, such as those from the Atmospheric Infrared Sounder (AIRS, Chahine et al., 2006)) aboard Aqua (Parkinson, 2003). Feng et al. (2021) further developed a synergistic method that incorporates cloud measurements of collocated active cloud profilers. By conducting a simulation experiment, Feng et al. (2021) demonstrated that this method can capture the

https://doi.org/10.5194/acp-2021-154
Preprint. Discussion started: 23 April 2021
© Author(s) 2021. CC BY 4.0 License.

variability of temperature and humidity above tropical convective storms and improve retrievals near the cloud top through the incorporation of active sensors.

In this study, we aim to quantify the effect of tropical cyclones on the TTL temperature, water vapor, and clouds using the A-Train satellite observations, specifically the infrared hyperspectra from AIRS and cloud profiles from CloudSat/CALIPSO. Tropical cyclones are of particular interest here because they constitute a large fraction of the most energetic (overshooting) convections in the tropics (Romps and Kuang, 2009) and provide vertically extended dense high clouds that enable the above-cloud temperature and humidity retrieval method developed by Feng et al. (2021). By using satellite observational datasets, which are introduced in Section 2, we aim to understand: 1) how tropical cyclones, especially the overshooting events, impact the TTL cloud occurrence and cloud ice (see Section 3.1 and 3.2), 2) whether tropical cyclones lead to an overall hydration in the TTL (see Section 3.3), and 3) how tropical cyclones affect the radiative heating in the TTL (Section 4). These questions are further discussed and concluded in Section 5.

2 Data and Methodology

2.1 Dataset

Following a sun-synchronized orbit with a repeat-cycle of 16 days, the A-Train satellites cross the equator at around 1:30 pm solar time in the ascending nodes and 1:30 am in the descending nodes every day.

CloudSat (Stephens et al., 2008) uses a cloud profiling radar operating at 94-GHz to observe cloud and precipitation. Sampling along-track at every 1.1 km, each measurement has a cross-track resolution of 1.4 km and along-track resolution of 1.8 km. With a vertical resolution of around 500 m, CloudSat provides several products (version P1_R05), including cloud water content (2B-CWC-RVOD), cloud classification(2B-CLDCLASS-LIDAR), and radiative heating rates (2B-FLXHR-LIDAR). In the 2B-CLDCLASS-LIDAR product, eight cloud types are classified, including cirrus, altostratus, altocumulus, stratus, stratocumulus, cumulus, nimbostratus, and deep convective clouds, depending on the vertical distribution of hydrometeors inferred from radar signal intensity and also their horizontal length scales (Wang and Sassen, 2007). The heating rate profiles in 2B-FLXHR-LIDAR (L'Ecuyer, 2007) are derived from two-stream broadband radiative transfer calculation combining cloud water content profile in 2B-CWC and atmospheric state profiles (temperature, water vapor, and ozone) from the ECMWF forecast, which are included in the ECMWF-AUX product (Partain, 2004).

The DARDAR (raDAR/liDAR, Delanoë and Hogan, 2008, 2010) product is based on the joint retrieval of ice clouds by using radar reflectivity measurements from CloudSat and lidar attenuated backscatter measurements obtained from CALIPSO (Cloud, Aerosol Lidar and the Infrared Pathfinder Satellite Observations, Winker et al., 2010) in synergy. Combining these two active instruments, DARDAR is sensitive to both optically thin cirrus in TTL and optically thick deep convective clouds (DCC). It provides the ice water content (IWC), the effective radius of ice particles, and the visible optical depth of ice clouds, at each CloudSat footprint spaced every 1.1 km.

In this study, we obtain the IWC profiles from the DARDAR-Cloud product (v2.1.0) and the cloud types from the CloudSat 2B-CLDCLASS-LIDAR product. Discrepancies exist between the CloudSat 2B-CLDCLASS-LIDAR and DARDAR products

https://doi.org/10.5194/acp-2021-154
Preprint. Discussion started: 23 April 2021
© Author(s) 2021. CC BY 4.0 License.

in terms of ice cloud existence. To overcome the discrepancies, a cloud layer detected by DARDAR but not classified in 2B-CLDCLASS-LIDAR is treated as the same cloud type as its adjacent cloud layer, or cirrus, if it is isolated.

The Aura Microwave Limb Sounder (MLS, Waters et al., 2006) retrieves water vapor above 316 hPa with a vertical resolution of around 3 km. The documented accuracy of version 4.2 product at the level of 100 hPa is 8% for water vapor. Although MLS can retrieve atmospheric states in moderately cloudy conditions, line shape distortion caused by the strong scattering of thick clouds limits the retrieval capability (Livesey et al., 2017). Therefore, only data not affected by clouds, based on a $status$ flag of the product, are used to avoid degraded data quality. Moreover, due to the limb-viewing scanning geometry, MLS has a relatively large sampling footprint with a horizontal resolution around 200 km along the track, which limits its sensitivity to the small-scale variability (Schwartz et al., 2013).

AIRS measures infrared spectra from 650 cm^{-1} to 2665 cm^{-1} with 2378 channels, using cross-track scans to provide a large spatial coverage of the measurements. Only the field-of-views (FOVs) with viewing angles within 15° from the nadir are used, considering that the limb-view geometry increases the optical depth and the atmospheric attenuation. The selected viewing angle corresponds to a cross-track span of around 400 km. The high spectral resolution in the mid-infrared makes it sensitive to temperature, water vapor, and also the cloud. However, the standard AIRS retrieval is not sensitive to the water vapor signal from the extremely dry UTLS region (Fetzer et al., 2008; Gettelman et al., 2004; Read et al., 2007). Moreover, the cloud-clearing retrieval method adopted by the AIRS standard retrieval suffers from large uncertainties in the overcast condition. Therefore, instead of using the AIRS Level 2 product for above-cloud atmospheric conditions, we apply a synergistic, cloudy-sky retrieval method developed from the cloud-assisted method proposed by Feng and Huang (2018). This retrieval method jointly uses the AIRS L1B v5 radiance measurements to retrieve water vapor and temperature above dense high-level clouds in FOVs where collocated DARDAR-Cloud contains thick upper-tropospheric clouds. It is hereinafter referred to as either joint AIRS-DARDAR retrieval or synergistic retrieval. This method is validated in Feng et al. (2021) and is found to be sensitive to the spatial variability in thermodynamic conditions above deep convections through a simulation experiment. The details of this retrieval method are presented in Appendix A.

The impact of cyclones is assessed by the anomalies in clouds and non-cloud variables compared to their climatologic values. In this paper, we define the climatology as the multi-year monthly mean of variables from 2006 to 2016, using the temperature from AIRS l2 v6, water vapor from MLS v4.2, the brightness temperature from AIRS L1B v5, and the IWC from DARDAR on a $1^o \times 1^o$ longitude-latitude grid, unless specified otherwise.

2.2 Compositing method

In this study, a list of tropical cyclones overpassed by the A-Train satellites is obtained from the CloudSat tropical cyclone product (2D-TC, Tourville et al., 2015). This product uses best-track information provided from the Automated Tropical Cyclone Forecasting System (Tourville et al., 2015; Sampson and Schrader, 2000) to identify the cyclone center position. Note that only daytime measurements are available after April 17th, 2011, due to a spacecraft battery issue. In addition to CloudSat, we combine CALIPSO, MLS, and AIRS together to provide the cloud distribution and atmospheric states associated with each cyclone overpass.

https://doi.org/10.5194/acp-2021-154
Preprint. Discussion started: 23 April 2021
© Author(s) 2021. CC BY 4.0 License.

Atmospheric Chemistry and Physics Discussions

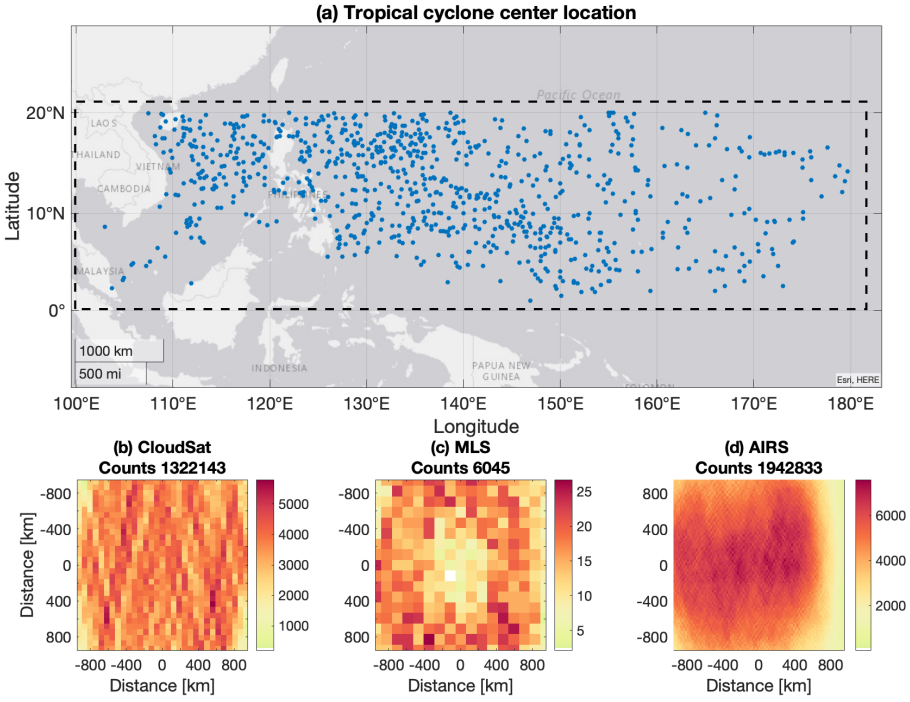

Figure 1. Distributions of cyclone centers overpassed by A-Train and sample density of A-Train instruments with respect to cyclone center locations. (a) Center locations of tropical cyclones (947 in total) overpassed by the A-Train satellites, over the northern part of the West-Pacific region (within the boxed area) from 2006 to 2016. The measurement sample density of (b) CloudSat (DARDAR product is available at the horizontal footprints of CloudSat), (c) MLS, and (d) AIRS (limited to viewing angles within 15° from the nadir). The sample densities are measured as the number of samples per 100 $\mathrm{km} \times 100$ km and shown at a resolution of 60 km, 120 km, and 20 km, respectively, for the three instruments. The numbers on the top of each panel show the total number of samples.

Measurements are composited with respect to cyclone center locations on the northern part of the West-Pacific region (the boxed region in Fig. 1 (a)) for the abundance of data samples in this region. The density of measurement locations of each instrument is shown in Fig. 1. The samples of AIRS (Fig. 1 (d)) are of higher density compared to CloudSat (Fig. 1 (b)) and MLS (Fig. 1 (c)) owing to the advantage of the cross-track scanning of AIRS. Considering that the sample densities and the FOV sizes of the original measurements of these instruments are different, the cyclone-centered composites are constructed by averaging variables over different spatial scales: 60 km (CloudSat and DARDAR), 120 km (MLS), and 20 km (AIRS), to ensure sufficient samples are obtained. Only oceanic observations are used to avoid sample discrepancies arising from land-sea contrast. Fewer nighttime measurements are available because of the daylight-only operation of CloudSat after 2011.

https://doi.org/10.5194/acp-2021-154
Preprint. Discussion started: 23 April 2021
© Author(s) 2021. CC BY 4.0 License.

3 Tropical cyclone impacts

3.1 Cloud distribution

The datasets introduced earlier are used to depict the cloud distributions above cyclones. DCCs and TTL clouds are especially of interest here. DCCs are classified in the CloudSat 2B-CLDCLASS-LIDAR dataset based on several conditions, including a vast horizontal and vertical extent, dense hydrometers, as inferred from radar reflectivity near the cloud top, and also the presence of precipitation (Wang and Sassen, 2007). TTL clouds, for the convenience of the analysis, are defined as clouds above 16 km, where the clear-sky LZRH and the mean tropopause (WMO, 1957) height typically locates in the tropics (Yang et al., 2010).

The occurrence frequency of clouds is then calculated as the ratio between the number of samples with a certain feature, e.g., TTL clouds, and the number of overpass samples in each 60 km ×60 km grid box in the cyclone-centered composite domain (Fig. 2 (a-b)). Using IWC profiles from the DARDAR-Cloud, a composite of ice water path (IWP) is derived in the same grid boxes. These results are also shown as a function of radial distance to the cyclone center in Fig. 3 (a-c).

Fig. 2 (a) and Fig. 3 (a) show that TTL clouds occur frequently above tropical cyclones. In the 2000 km × 2000 km cyclone-centered composite domain, TTL clouds have an occurrence frequency of 0.37 on average, which is significantly greater than the climatology value of 0.03. This climatology value is derived from the DARDAR-Cloud from 2006 to 2016, regardless of the presence of cyclones. DCCs occur mostly within 400 km from the cyclone center (Fig. 3 (a)) and are noticeably more often on the southwest side of the cyclones (Fig. 2 (b)). The occurrence frequency of DCCs in the composite domain is 0.1 on average, while the climatology value (regardless of cyclone condition) is only 0.008. These results suggest that tropical cyclones considerably increase the occurrences of both DCCs and TTL clouds.

In contrast to the uniformly distributed TTL cloud (Fig. 2 (a)), Fig. 2 (c) shows that the TTL cloud ice is concentrated in regions closest (within 200 km) to the cyclone center, preferably to the southwest, similar to the DCCs (Fig. 2 (b)). This coincidence suggests a linkage between TTL cloud ice and DCCs that penetrate the bottom of TTL (the 16 km altitude). We refer to them as the "overshooting" DCCs in the context of this paper.

TTL clouds then are broken into four categories to distinguish TTL clouds with or without underlying deep convections. As shown by the schematic in Fig. 4, the four cloud categories are defined as follows:

- DCC-OT: overshooting DCCs, whose top boundary exceeds 16 km.
- DCC-NOT: non-overshooting DCCs, whose top boundary is below 16 km, while cloud detected above 16 km.
- CI: cirrus detected above 16 km and no DCC or any other cloud in the column.
- MIX: the remaining conditions (no DCC, but cloud detected above 16 km).

For convenience, TTL cloud categories without overshooting, including DCC-NOT, CI, and MIX, are also referred to as TTL-OTHER. Clouds with their top boundary below 16 km are referred to as NTTL.

https://doi.org/10.5194/acp-2021-154
Preprint. Discussion started: 23 April 2021
© Author(s) 2021. CC BY 4.0 License.

Atmospheric Chemistry and Physics
Discussions

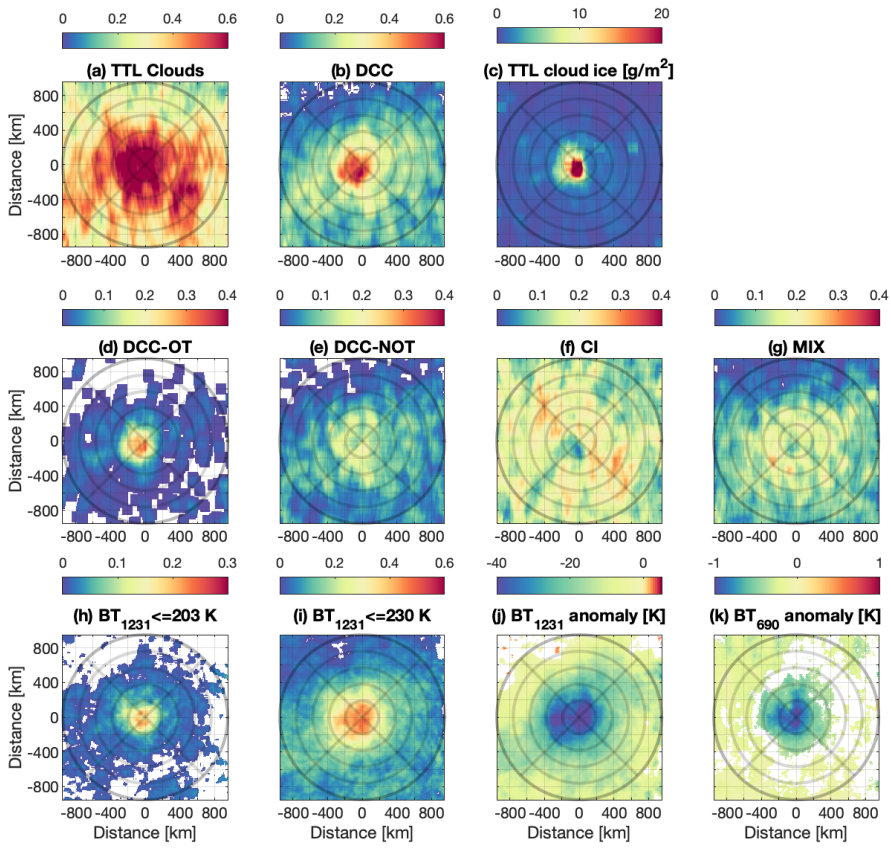

Figure 2. Cyclone-centered composite of cloud statistics.

(a) The occurrence frequency of TTL clouds (i.e., clouds above 16 km) and (b) deep convective clouds (regardless of TTL cloud occurrences).

(c) Ice water path (g/m^2) above 16 km.

The occurrence frequency of four cloud categories (schematically shown in Fig. 4): (d) DCC-OT, (e) DCC-NOT, (f) CI, and (g) MIX.

The occurrence frequency of clouds identified by infrared radiance measurements: (h) deep convective clouds with $BT_{1231} <= 203$ K and (i) overcast high cloud with $BT_{1231} <= 230$ K.

(j) Brightness temperature anomaly [K] in atmospheric window channel (BT_{1231}) and (k) CO_2 channel (BT_{690}).

Upper (a-c), middle(d-g), and lower (h-k) panels are based on data from DARDAR cloud-IWC, CloudSat-2B CLDCLASS-LIDAR, and AIRS L1B product, respectively. Only statistically significant occurrences (at a 99% confidence level, compared to zero) are shown in (a,b,d-i), and only significant brightness temperature anomalies (99%, compared to the climatology) are shown in (j,k).

https://doi.org/10.5194/acp-2021-154
Preprint. Discussion started: 23 April 2021
© Author(s) 2021. CC BY 4.0 License.

Atmospheric Chemistry and Physics Discussions

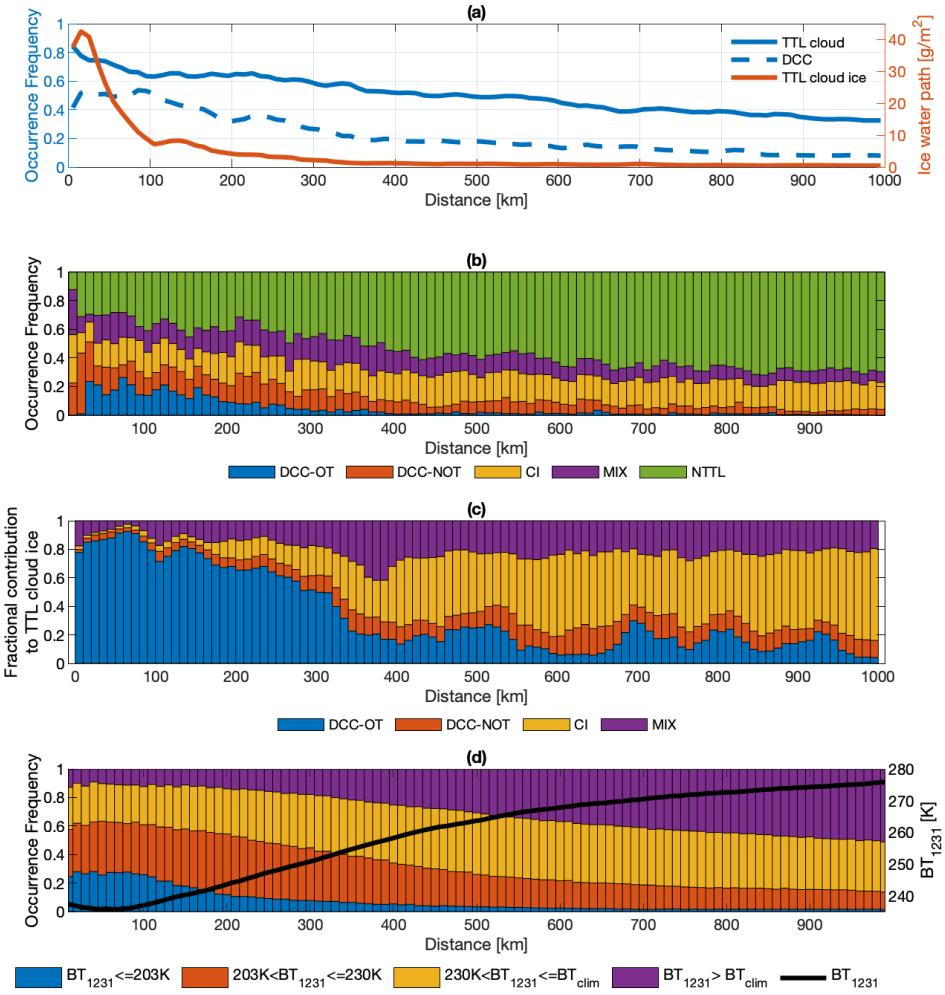

Figure 3. Cloud statistics as a function of radial distances to cyclone center.

(a) Occurrence frequency of TTL clouds (blue solid curve) and deep convective clouds (blue dashed curve); the red curve is the ice water path ($\mathrm{g/m^2}$) above 16 km.

(b) Occurrence frequency of each cloud category (schematically shown in Fig. 4).

(c) Fractional contribution to the TTL cloud ice (the red curve in panel (a)) by each cloud category.

(d) Occurrence frequencies of clouds classified by BT_{1231}. BT_{clim} refers to the multi-year monthly mean BT_{1231}. The black curve shows the average BT_{1231}.

https://doi.org/10.5194/acp-2021-154
Preprint. Discussion started: 23 April 2021
© Author(s) 2021. CC BY 4.0 License.

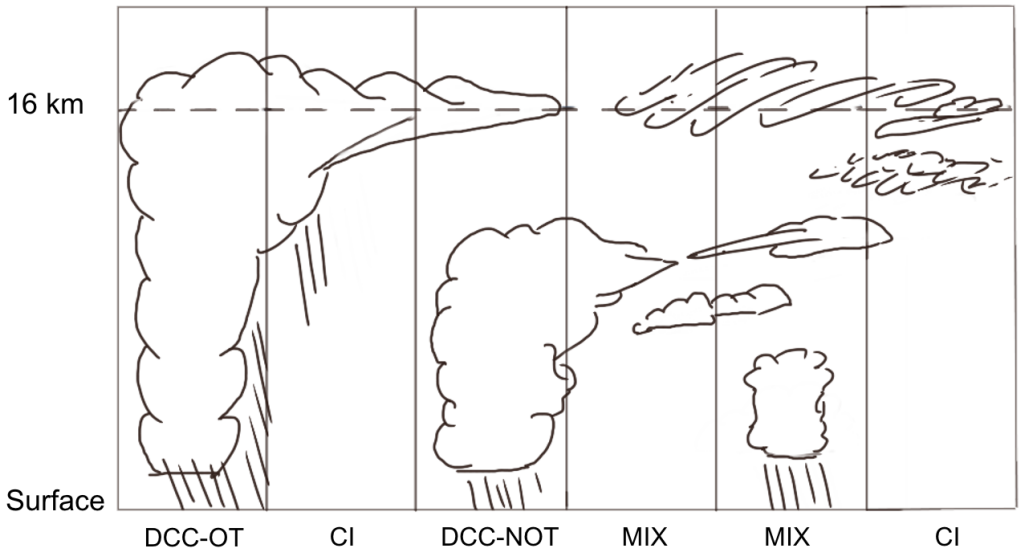

Figure 4. A schematic of the TTL cloud categories (see definitions in Section 3.1).

As depicted by Fig. 4, we distinguish the DCC-OT and DCC-NOT by whether the lowermost TTL clouds are connected with underlying DCCs, because the adjacent clouds are essentially considered as the same cloud type in the CloudSat cloud classification dataset (2B-CLDCLASS-LIDAR). Columns with only cirrus clouds are classified as CI. In the MIX category, the TTL clouds may lie over either middle clouds (accounting for 90% of the MIX category) or low clouds (10% of the MIX category). MIX and CI categories also include optically thick anvil clouds near the edge of DCCs, because anvil cloud is classified as cirrus or altostratus in the 2B-CLDCLASS-LIDAR(Wang and Sassen, 2007; Young et al., 2013), depending on its vertical position,

Following this classification, we compute the occurrence frequency of each cloud category and their fractional contribution to TTL cloud ice. The fractional contribution to TTL cloud ice in a grid box is calculated as the ratio between the sum of TTL cloud ice of one cloud category and the total TTL cloud ice. DCC-OTs frequently occur within the 400 km radius, accounting for the majority of TTL cloud ice (Fig. 3 (c)). CI category has an occurrence frequency generally over 0.2, which makes up over 60% of the total TTL clouds occurrence outside the 400 km radius (Fig. 2 (f) and Fig. 3 (b)), but contributes little to the TTL cloud ice (Fig. 3 (c)). Overall, Fig. 2 and 3 depict that most TTL clouds above cyclones are of the CI type, while the TTL cloud ice is dominantly contributed by overshooting deep convections (DCC-OT).

https://doi.org/10.5194/acp-2021-154
Preprint. Discussion started: 23 April 2021
© Author(s) 2021. CC BY 4.0 License.

3.2 Infrared Radiance

In the previous section, the distribution patterns of cloud above tropical cyclones are analyzed by combing observational products from CloudSat and CALIPSO. Compared with the nadir-view-only instruments, AIRS provides continual spatial coverage by performing a cross-track scan. With over two thousand channels, this hyperspectral instrument sounds atmospheric absorbers and temperatures at different altitudes. For example, the brightness temperature (BT) at the atmospheric window channel is sensitive to the cloud top temperature for inferring the cloud top height.

As discovered in Section 3.1, overshooting DCCs are a major source of the TTL cloud ice. The spectral signatures of the overshooting DCCs are further investigated. Previous studies (Aumann et al., 2011; Aumann and Ruzmaikin, 2013) have shown that overshooting DCCs are identifiable by cold BT anomalies in the window channels, e.g., at the 1231 cm^{-1} channel (BT_{1231}) and also positive BT difference between the water vapor and window channels ($\Delta BT = BT_{1419} - BT_{1231}$), (Aumann et al., 2011; Aumann and Ruzmaikin, 2013). The cold BT_{1231} is a result of extremely high vertical reach (and thus the very low cloud top temperature) of the DCCs; the positive ΔBT indicates emission from warm stratospheric layers against the cold cloud top. However, there is no consensus on the threshold values of these quantities to identify DCCs, partly because of the uncertainty in the temperature distribution above the DCCs due to the impact of convection. Following the statistical analysis detailed in Appendix B, we find the optimal threshold for identifying overshooting DCCs to be $BT_{1231} <= 203$, corresponding to a false positive rate of 0.008 and a false negative rate of 0.323. We find that incorporating ΔBT does not improve the detection.

We then apply this $BT_{1231} <= 203$ K criterion to AIRS overpass measurements (Fig. 1 (d)). Figure 2 (h) shows that the identified deep convections by this criterion distribute similarly to the overshooting DCC (DCC-OT) classified by CloudSat. It also confirms a southwest preference for overshooting DCC to occur.

Similarly, a $BT_{1231} <= 230K$ criterion is used to identify thick upper-tropospheric clouds. This criterion detects cloud tops above 11 km, which corresponds to a climatologic mean temperature of 230 K. The identified upper-tropospheric clouds distribute mainly within the 400 km radius, as depicted in Fig. 2 (i), with a frequency of over 0.3. Figure 2 (i) also reveals fewer thick high clouds on the northwest side of the domain, similar to the results based on CloudSat data (Fig. 2 (e,g)). This BT_{1231} criterion is also used for identifying FOVs with thick upper-tropospheric clouds to perform the synergistic retrieval method discussed in Section 3.3.

For each AIRS overpass sample, the BT_{1231} anomaly is calculated as the deviation from the climatology. As shown in Fig. 2 (j), cyclones induce significant cold anomaly in BT_{1231} over the composite domain.

The reduced window channel radiance (BT_{1231}) suggests that cyclone clouds effectively attenuate the infrared radiation emitted from the surface, thus potentially leading to a net radiative cooling of the atmospheric layers above the clouds. Hence, it is interesting to examine whether tropical cyclones leave detectable signatures in the temperature fields. A composite of BT anomalies using a CO_2 absorption channel (690 cm^{-1}) is shown in Fig. 2 (k). This channel has a weighting function that peaks at 85 hPa, thus being sensitive to the cold point temperature (i.e., the minimum temperature) which climatologically occurs near this level. Indeed, Fig. 2 (k) shows a cold BT_{690} above cyclones, especially around the cyclone center. However,

https://doi.org/10.5194/acp-2021-154
Preprint. Discussion started: 23 April 2021
© Author(s) 2021. CC BY 4.0 License.

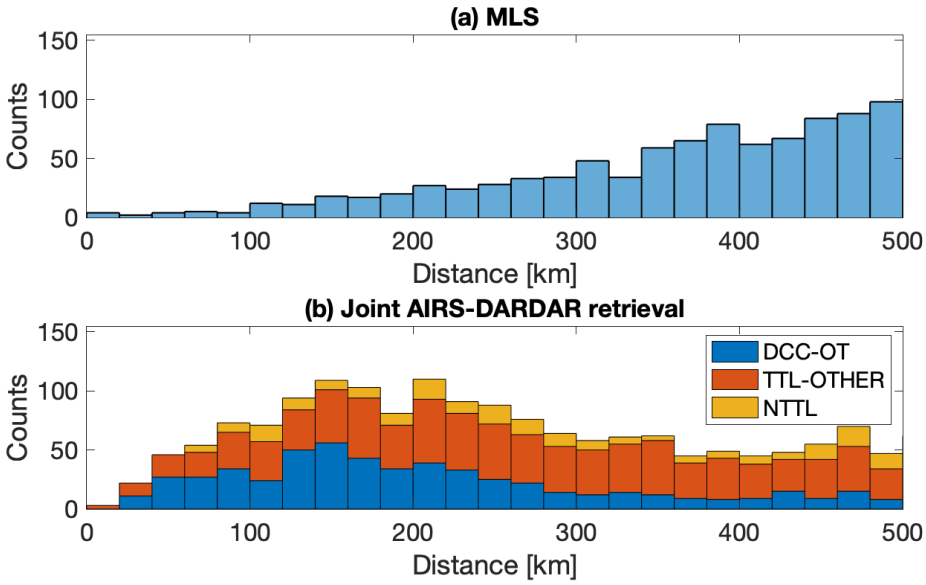

Figure 5. Samples densities used for assessing temperature and humidity distributions from (a) MLS and (b) joint AIRS-DARDAR retrieval.

we cannot eliminate the possible impacts of cloud emission, which will be addressed in the following section using different methods, including a synergistic retrieval that we developed using the A-Train data.

3.3 Temperature and water vapor

In the previous sections, we find substantial increases in cloud occurrence and cloud ice above tropical cyclones. While the increase of TTL clouds is direct evidence of cross-tropopause transports, previous studies (Ueyama et al., 2018; Schoeberl et al., 2018) have suggested that the TTL cloud ice can lead to either hydration or dehydration, depending on the pre-existing conditions. Hence, it is important to examine the water vapor field above the cyclones to ascertain the (de)hydration impact.

A joint AIRS-DARDAR retrieval method has been developed to retrieve atmospheric conditions above thick upper-tropospheric clouds, combining hyperspectral infrared radiances from AIRS and collocated IWC profiles from DARDAR-Cloud. The retrieval method was described in detail and validated using a simulation experiment in (Feng et al., 2021). In summary, the retrieval can achieve a precision of 0.31 K and 0.36 ppmv for temperature and water vapor at 100 hPa, respectively. Additional information is provided in Appendix A to explain how the temperature and water vapor above tropical deep convections are retrieved.

The AIRS FOVs selected for the synergistic retrieval are within 6.75 km (half of AIRS nadir footprint size) to the nearest DARDAR cloud profile and have window band brightness temperature (BT_{1231}) colder than 230 K. The BT_{1231} threshold ensures that liquid clouds can be neglected in the retrieval. The frequency of AIRS FOVs passing this criterion is shown in Fig. 2 (i) and Fig. 3 (d). The selection of FOVs is illustrated in Fig. 6 for a tropical cyclone event. In this figure, the brightness

https://doi.org/10.5194/acp-2021-154
Preprint. Discussion started: 23 April 2021
© Author(s) 2021. CC BY 4.0 License.

temperature in a window channel from AIRS L1B observation depicts a typical cyclonic cloud distribution. The vertical cross-section illustrates the retrieval over selected AIRS FOVs. The same data selection and retrieval processes are performed for all tropical cyclone overpasses. In total, 3475 FOVs from 345 tropical cyclone events are selected and among them, 2735 profiles are successfully retrieved (reaching convergence in the iterative retrieval procedure). The converged retrievals mostly locate within 500 km from the cyclone center; their distributions are shown in Fig. 5 (b). The constructed cyclone-centered composites of retrieved temperature, water vapor, and cloud, are shown as a function of vertical level and radial distance in Fig. 7 (a,e).

Owing to smaller horizontal sampling footprints and the availability of collocated cloud observations, the synergistic retrieval can reveal the small-scale variations in the thermodynamic fields above TTL clouds. In order to understand whether overshooting convections have a direct impact on water vapor, retrieved samples are classified into overshooting DCCs (DCC-OT) and non-overshooting TTL clouds (TTL-OTHER), and non-TTL clouds (NTTL), using the same cloud classification introduced in Section 3.1. The converged profiles contain 731 DCC-OTs, 1508 TTL-OTHERs, and 496 NTTLs; their sample densities are shown in Fig. 5 (b). The mean profiles for each category are shown in Fig. 9 (a,b).

Meanwhile, similar cyclone-centered composites of thermodynamic fields are constructed using MLS v4.2 and ERA5 (Hersbach et al., 2020) in Fig. 7. The sample locations of ERA5 are identical to the measurement locations used for the synergistic (joint AIRS-DARDAR) retrieval. The measurement locations of MLS products used in this study are shown in Fig. 1 (c) and Fig. 5 (a). The sample density of MLS near the cyclone center is lower because only measurements not affected by high clouds are used. Figure 7 also shows composites of IWC, from the synergistic retrieval (Fig. 7 (a,e)), DARDAR-Cloud (Fig. 7 (b,f), corresponding to measurements shown in Fig. 1 (b)), and ERA5 (Fig. 7 (c,g)) at retrieved sample locations, respectively. We note that there is no collocation between DARDAR-Cloud and MLS in Fig. 7 (b,f) as only MLS observations not impacted by high clouds are selected.

The effects of cyclones on temperature and water vapor are examined by subtracting the multi-year monthly mean at every sample location from Fig. 7. The anomalous thermodynamic fields are presented in Fig. 8, while the mean anomalies for three cloud categories (DCC-OT, TTL-OTHER, and NTTL) are shown in Fig. 9 (c,d). For MLS and ERA5, the monthly mean climatologies are constructed using the same dataset (MLS or ERA5, respectively). For the synergistic retrieval, there is no available 'climatology' from this retrieval dataset for non-cyclonic conditions. AIRS L2 temperature and MLS water vapor products are used instead, which are converted to the same vertical resolution to reduce the systematic bias, as described in Appendix A.

3.3.1 Temperature

Using the synergistic retrieval, we find that tropical cyclone events lead to an oscillating pattern of temperature anomalies above the cloud top (Fig. 8 (a)). This shifts the cold-point tropopause to higher altitudes (see also Fig. 9 (a)). Compared to the climatology, the mean temperature profile above cyclones shows a noticeable negative anomaly between 40 to 100 hPa and positive anomalies at other vertical ranges. We note that this cold anomaly around 80 hPa also confirms the cold signature in

https://doi.org/10.5194/acp-2021-154
Preprint. Discussion started: 23 April 2021
© Author(s) 2021. CC BY 4.0 License.

Atmospheric Chemistry and Physics Discussions

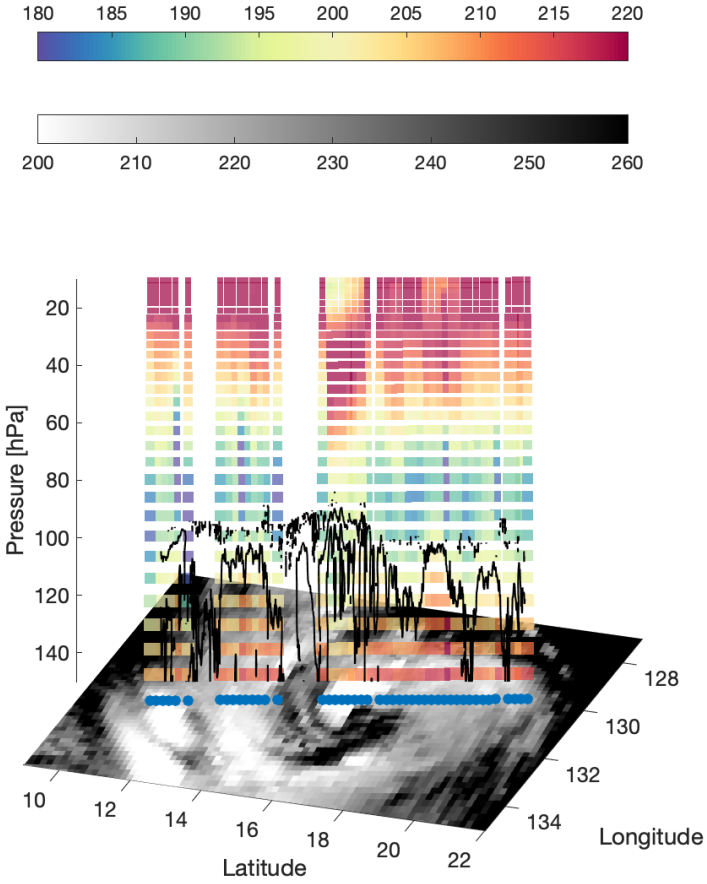

Figure 6. A-Train overpass and retrieval in a tropical cyclone event on October 2nd, 2007. The underlying image in greyscale shows the brightness temperature at a window channel (BT_{1231},[K]) from the AIRS L1B v5 product and indicates the cloud-top temperature. The vertical cross-section in color contour illustrates the temperature ([K]) retrieval, over thick upper-tropospheric clouds (BT_{1231} colder than 230 K) using the synergistic method described in the texts; the black line marks the IWC at 10^{-4} $\mathrm{g/m^3}$ based on the DARDAR data and outlines the cloud top positions.

https://doi.org/10.5194/acp-2021-154
Preprint. Discussion started: 23 April 2021
© Author(s) 2021. CC BY 4.0 License.

Atmospheric Chemistry and Physics Discussions

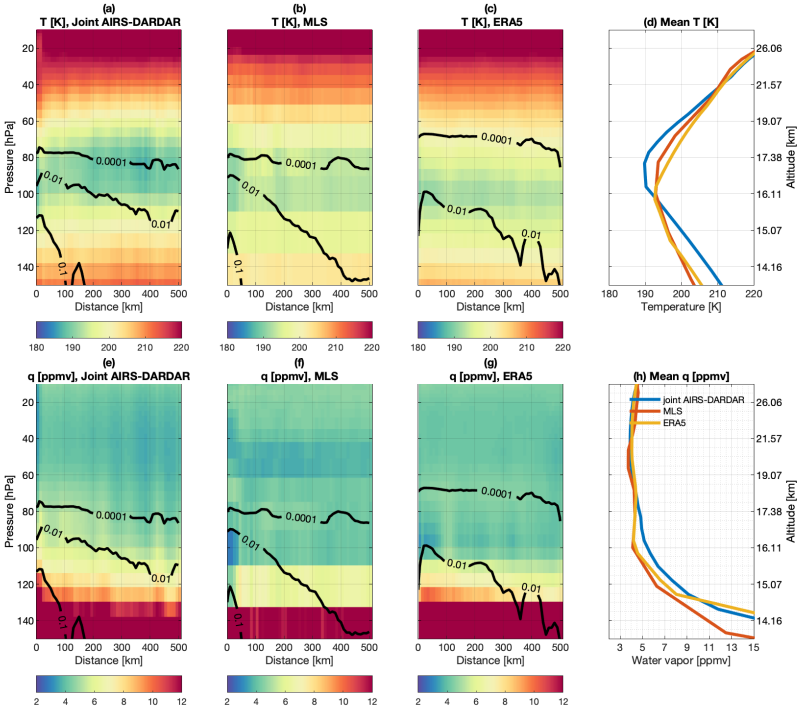

Figure 7. Cyclone-centered composites of temperature [K], water vapor [ppmv], and ice water content [g/m^3].
Temperature (a) and water vapor (e) from joint AIRS-DARDAR retrieval; the counts of samples are shown in Fig. 5 (b).
Temperature (b) and water vapor (f) from MLS v4.2 product; the counts of samples are shown in Fig. 1 (c) and Fig. 5 (a). The IWC is from DARDAR-Cloud; the sample density is shown in Fig. 1 (a)
Temperature (c) and water vapor (g) from ERA5 product sampled at the same locations as (a,e).
Mean temperature (d) and water vapor (h) profiles from different datasets.

BT_{690} displayed in Fig. 2 (k). This vertically oscillating anomaly feature is consistent with previous findings using radiosonde and GPS radio occultation measurements (Holloway and Neelin, 2007; Biondi et al., 2013; Rivoire et al., 2016).

The oscillating pattern of temperature anomalies may be caused by a few reasons. The good alignment of the cold anomaly with the cloud top position around the cold point ($\sim$80 hPa) signifies the impact of cloud radiative effects. This motivates us to ascertain the role of radiation in forming the retrieved temperature pattern. The thick cloud layers may absorb the incoming solar radiation to heat the cloud top while attenuating the emission from the warm surface to cool the atmospheric layers above the cloud. These expected cloud radiative effects agree with the signs of temperature anomalies and will be further examined in Section 5. On the other hand, Rivoire et al. (2020) pointed out that the cloud radiative cooling only partly explains the cooling tendency above cyclones. Other mechanisms at play may include the adiabatic expansion (Holloway and Neelin, 2007) of the convective overshoots (Robinson and Sherwood, 2006) and the outward branch of the secondary circulation (Rivoire et al., 2020; Schubert and McNoldy, 2010).

https://doi.org/10.5194/acp-2021-154
Preprint. Discussion started: 23 April 2021
© Author(s) 2021. CC BY 4.0 License.

Atmospheric Chemistry and Physics Discussions

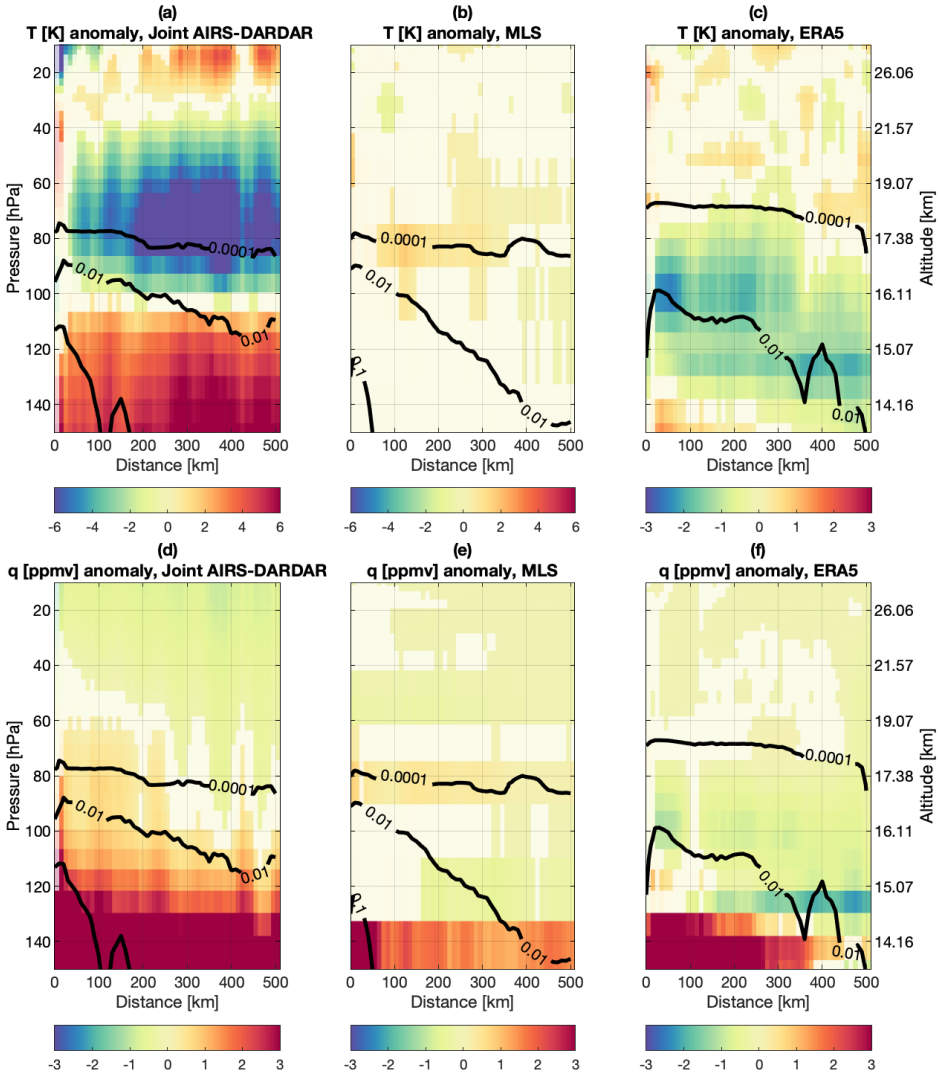

Figure 8. Temperature and water vapor anomalies above tropical cyclones. Anomalies below 99% confidence level are set to be transparent.

(a,d) Similar to Fig. 7 (a,e) but after subtracting the climatologies of temperature from AIRS L2 v6 product and water vapor from MLS v4.2 product, respectively.

(b,e) Similar to Fig. 7 (b,f) but after subtracting the climatologies of temperature and water vapor from MLS v4.2 product.

(c,f) Similar to Fig. 7 (c,g) but after subtracting the climatologies of temperature and water vapor from ERA5.

https://doi.org/10.5194/acp-2021-154
Preprint. Discussion started: 23 April 2021
© Author(s) 2021. CC BY 4.0 License.

It is also interesting to find that the temperature anomaly is stronger above non-overshooting clouds (TTL-OTHERs), in comparison with DCC-OTs and NTTLs (Fig. 9 (a,c)). It suggests a potential linkage between the temperature anomaly and the formation of TTL clouds. For example, one plausible explanation is that the cooling of air above cyclones promotes the formation of thicker TTL clouds by depositing the pre-existing water vapor onto ice particles, which are evident in Fig. 9 (d) and Fig. 10 as discussed in Section 3.3.2.

We note that the significant temperature anomaly pattern disclosed by the synergistic retrieval is not found in either MLS or ERA5. Livesey et al. (2017) have documented that MLS temperature retrieval is particularly susceptible to cloud contamination, while Schwartz et al. (2008) note that this issue cannot be effectively screened out by the $status$ flag of the MLS v4.2 product. Therefore, the MLS temperature product may not be able to observe the pattern of temperature anomaly.

By comparing ERA5 (Fig. 7 (c) and Fig. 8 (c)) to the synergistic retrieval (Fig. 7 (a) and Fig. 8 (a)), we find that ERA5 produces a higher cloud top (marked by 10^{-4} $\mathrm{g/m^3}$ IWC contour) than the DARDAR observation but in general underestimates the TTL cloud ice. ERA5 also exhibits a cold anomaly but places it in lower altitudes compared to the synergistic retrieval, which is partly attributable to different radiative heating due to differences in cloud ice. Previous studies (Wright et al., 2020) have also found large discrepancies in the upper-tropospheric temperature and tropical high clouds among reanalysis products, likely due to convective parameterization (Takahashi et al., 2016; Wright et al., 2020).

3.3.2 Water Vapor

Using the synergistic retrieval, Fig. 8 (d) shows that both hydration and dehydration can occur above cyclones. Hydration is found below 80 hPa, especially near the cyclone center, while dehydration is found above 60 hPa. This finding is consistent with MLS observation (Fig. 8 (e)), despite that synergistic retrievals are performed above thick upper-tropospheric clouds while the selected MLS observations are high-cloud free.

We note that the synergistic retrieval does not have a high vertical resolution to fully resolve the vertical distribution of water vapor, due to the smearing effect of the averaging kernel discussed in Appendix A. Nevertheless, the retrieval is sensitive to the spatial variability of the column integrated water vapor (CIWV), which is validated in Feng et al. (2021) and Appendix A. The retrieved CIWV above 16 km is shown in Fig. 10 (a, b), as a function of radial distance to cyclone center. Therefore, we focus on the horizontal variability in CIWV above cyclones, which can be more confidently detected by the synergistic retrieval, to disclose overall hydration or dehydration above 16 km.

The synergistic retrieval detects a decreasing CIWV with the increasing radial distances (Fig. 10 (a,b)). Significant hydration occurs near the cyclone center, increasing the CIWV by up to 0.18 $\mathrm{g/m^2}$, while dehydration occurs around a distance of 375 km. In MLS, the CIWV does not substantially differ from the climatology, possibly because MLS samples large, high-cloud free areas.

The (de)hydration impact of cyclones is separated after isolating DCC-OTs, TTL-OTHERs, and NTTLs. As depicted in Fig. 10 (a,b), significant dehydration is only found above non-overshooting TTL clouds, while significant hydration is found above overshooting clouds and non-TTL clouds. DCC-OTs increase the CIWV above 16 km by up to 0.4 $\mathrm{g/m^2}$, which is equivalent to 20 $\%$ of the climatological value. It suggests that overall the air above cyclones is hydrated by the convection, especially

https://doi.org/10.5194/acp-2021-154
Preprint. Discussion started: 23 April 2021
© Author(s) 2021. CC BY 4.0 License.

Atmospheric Chemistry and Physics Discussions

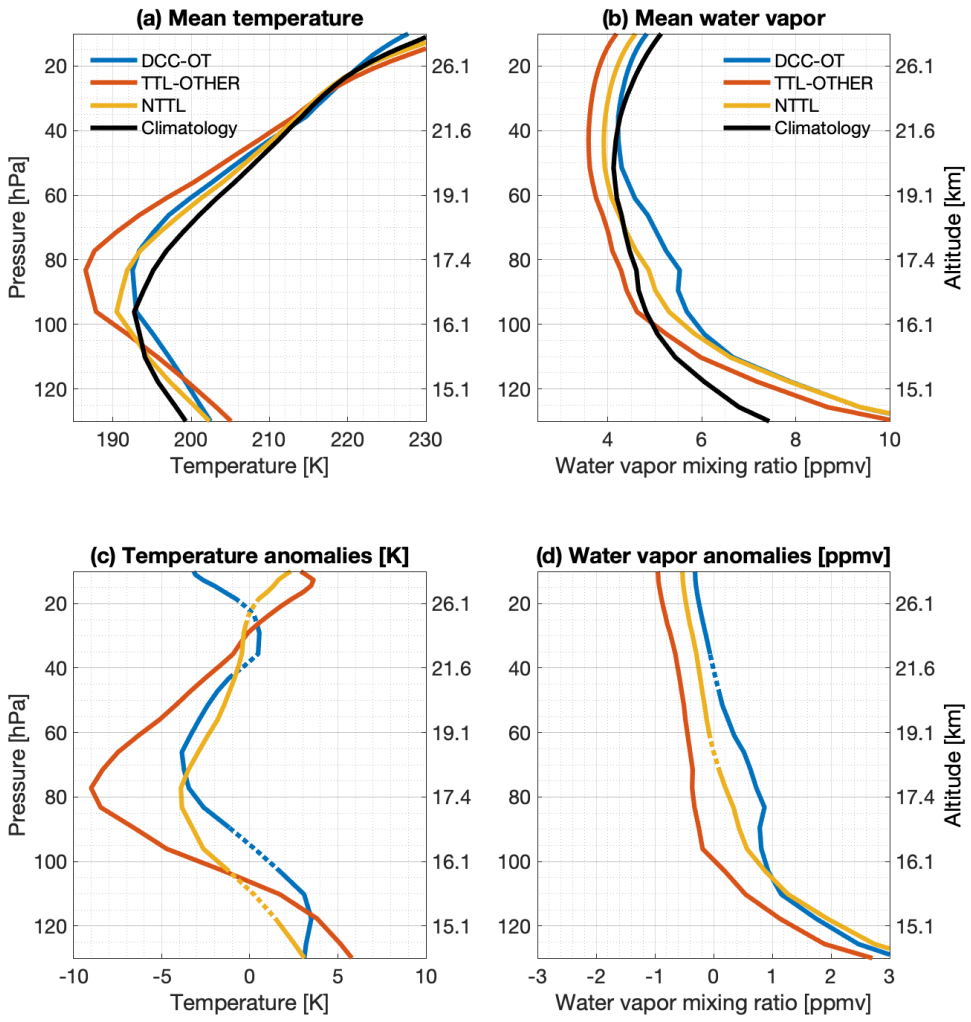

Figure 9. The mean (a) temperature [K) and (b) water vapor [ppmv] profiles above cyclones, for overshooting (DCC-OTs, blue), non-overshooting (TTL-OTHERs, orange) TTL clouds, and non-TTL clouds (NTTL, yellow), and the climatology (black). (c,d) the same as (a,b), but for anomalies, with respect to the climatology.

https://doi.org/10.5194/acp-2021-154
Preprint. Discussion started: 23 April 2021
© Author(s) 2021. CC BY 4.0 License.

Atmospheric Chemistry and Physics Discussions

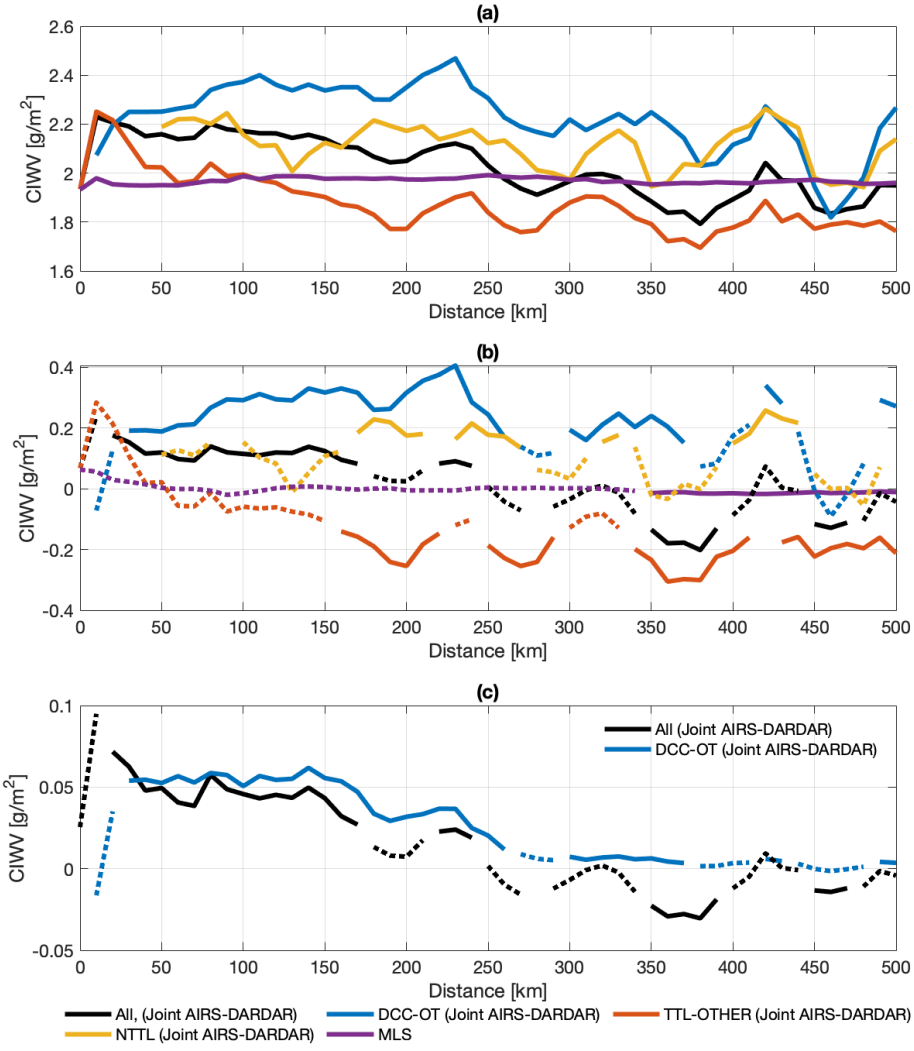

Figure 10. (a) Column integrated water vapor (CIWV) above 16 km from the joint AIRS-DARDAR retrieval (blue) and MLS (black). Samples retrieved by the synergistic retrieval are separated into overshooting (DCC-OT, red) and other non-overshooting clouds (yellow). Solid curves show the statistically significant (99% confidence level) anomaly and dashed curves are not statistically significant.

(b) Same as (a) except for the anomaly in CIWV.

(c) Contributions to the CIWV anomaly from thick upper-tropospheric clouds (BT_{1231}<230 K, blue) and DCC-OTs (red).

https://doi.org/10.5194/acp-2021-154
Preprint. Discussion started: 23 April 2021
© Author(s) 2021. CC BY 4.0 License.

the overshooting convection that penetrated the bottom of TTL. The role of non-overshooting TTL clouds (TTL-OTHER), however, is found to be associated with a dryer environment, possibly due to the deposition of water vapor onto ice particles in colder temperatures (as evident from Fig. 8 (a) and Fig. 9 (a,c)).

The occurrence frequency of thick upper-tropospheric clouds (AIRS FOVs being colder than 230 K), above which the synergistic retrieval is conducted, is shown in Fig. 3 (d). The expectation of changes in CIWV contributed by thick upper-tropospheric clouds is then estimated by multiplying the CIWV anomaly (Fig. 10 (b)) by the occurrence frequency of these clouds (Fig. 3 (d), blue and orange areas). Figure 10 (c) shows that the CIWV above cyclones is expected to be around 0.05 $\mathrm{g/m^2}$ (1.5%) higher than the climatology within a 150 km radius of the cyclone center, and to be up to 0.03 $\mathrm{g/m^2}$ (0.9%) lower at a distance of 375 km. On average, the stratospheric column above thick upper-tropospheric clouds within 500 km from cyclone centers is 0.014 $\mathrm{g/m^2}$ moister than the climatology. A similar calculation is performed for DCC-OTs, using the occurrence frequency of DCC-OTs shown by the blue area in Fig. 3 (b). It is found that DCC-OT alone increases the mean CIWV above tropical cyclones by 0.024 $\mathrm{g/m^2}$, which is around 0.7 $\%$ of the climatology value.

In summary, hydration is found to result from overshooting convection which injects water substance directly. The moisture injected by overshoots will hydrate the surrounding environment so that the cloud-free TTL (NTTLs) also shows higher CIWV compared to the climatology. However, at locations away from overshoots, we find that overflow or pre-existing clouds in the TTL are associated with a colder and drier environment, potentially due to water vapor deposition onto ice particles.

4 Radiative effects

In the context of this paper, we have defined the lower boundary of the TTL to be the clear-sky level of zero-radiative heating (LZRH). The radiative heating rates in the TTL are crucial, for instance, to the variations of stratospheric water vapor, as it radiatively drives the air parcel to diabatically ascend to the higher stratosphere. While the previous section has found the overall hydration effect of cyclones, we are interested in how the radiative heating rates are perturbed above tropical cyclones and whether this helps retain the moisture in TTL.

Moreover, as indicated by the good alignment of cloud boundary and temperature anomalies, the cloud radiative effects may have played a role in forming the temperature anomalies as seen in Fig. 8. Therefore, a cyclone-centered composite of radiative heating rates, using the CloudSat 2B-FLXHR-LIDAR product, is constructed to help address these questions.

The cloud radiative effect, measured by the radiative heating rate difference between all-sky and clear-sky overpasses, is shown as a function of pressure level and radial distance to the cyclone center in Fig. 11 (c,d). Only daytime samples (overpassing at 13:30 local solar time) are used, to exclude the lack of shortwave heating during the nighttime. We identify the LZRH in the heating rate profiles as the level where heating rates change from negative to positive. Note that there is no LZRH identified under two conditions: in Fig. 11 (a,c) when the longwave heating rate is all negative in the TTL, and in Fig. 11 (b,d,e) when the net heating rate is all positive.

In the longwave, Fig. 11 (c) shows that clouds generally heat inside the clouds (below 200 hPa) but cools the atmosphere near and above the cloud top (marked by the 0.01 $\mathrm{g/m^3}$ IWC contour). Figure 11 (d) shows that this longwave cooling effect is

https://doi.org/10.5194/acp-2021-154
Preprint. Discussion started: 23 April 2021
© Author(s) 2021. CC BY 4.0 License.

Atmospheric Chemistry and Physics Discussions

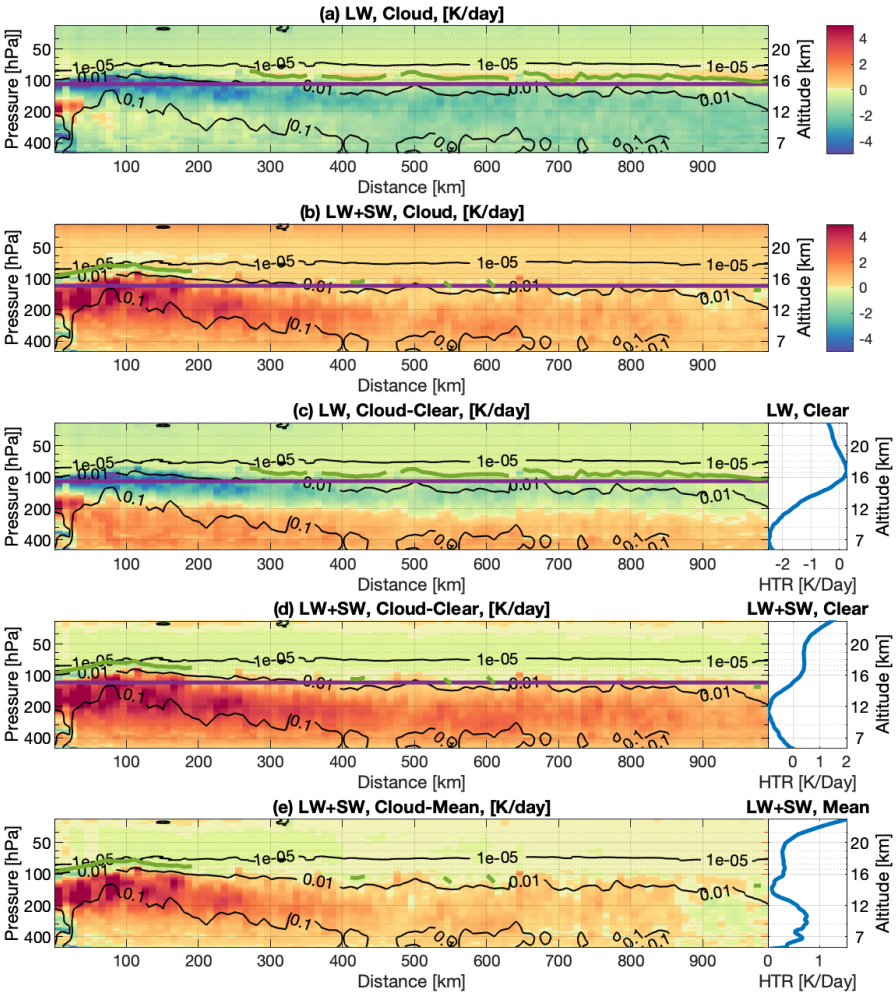

Figure 11. Cloud radiative heating [K/day] as a function of distance to cyclone center.

(a) Longwave and (b) net (longwave + shortwave) radiative heating rates from CloudSat 2B FLXHR-LIDAR.

(c,d) Same as (a,b) but for cloud radiative effects, which are defined as the differences between all-sky and the mean of clear-sky heating rate (blue curve in the right panel).

Black contour lines show the DARDAR ice water content (g/m^3). The Magenta line marks the clear-sky LZRH. The green line marks the cloudy-sky LZRH, determined as the vertical position where heating rate changes from positive to negative.

https://doi.org/10.5194/acp-2021-154
Preprint. Discussion started: 23 April 2021
© Author(s) 2021. CC BY 4.0 License.

Atmospheric Chemistry and Physics Discussions

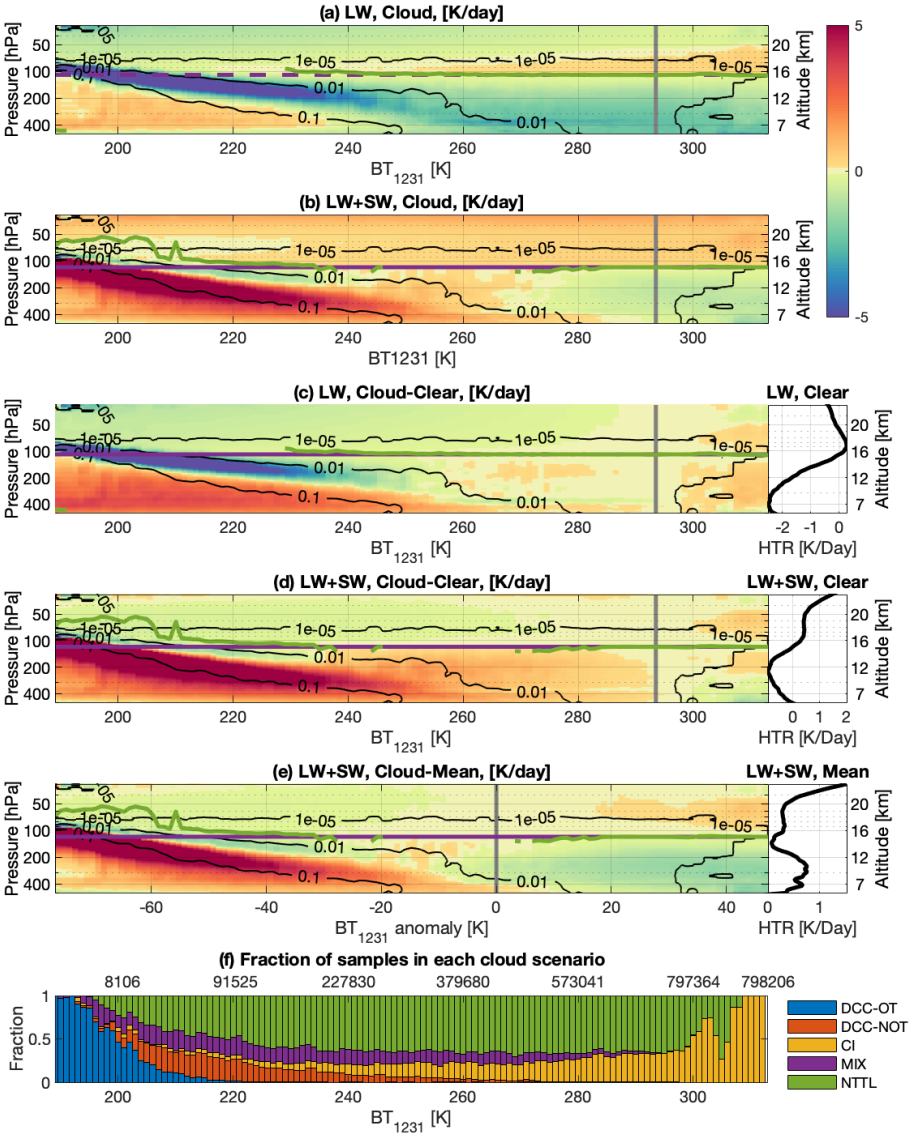

Figure 12. Cloud radiative heating rates [K/day] as a function of window band radiance, BT_{1231}, from collocated AIRS L1B v5.

(a) Longwave and (b) net (longwave + shortwave) radiative heating rates from CloudSat 2B FLXHR-LIDAR.

(c,d) Same as (a,b) but for cloud radiative effects, which is defined as the difference between all-sky and the mean of clear-sky heating rate (black curve in the right panel).

(e) Net cloud radiative heating rate anomaly difference between all-sky and the mean of all-sky cyclone overpass (black curve in the right panel).

(e) The proportion of samples in each cloud category (classified in Section 3.1) to all cloudy overpass samples. The numbers on the top indicate the number of cloudy samples with BT_{1231} colder than the corresponding temperature marked at the bottom.

Black contour lines show the DARDAR ice water content ($\mathrm{g/m^3}$). The Magenta line marks the clear-sky LZRH. The green line marks the cloudy-sky LZRH, determined as the vertical position where heating rate changes from positive to negative.

https://doi.org/10.5194/acp-2021-154
Preprint. Discussion started: 23 April 2021
© Author(s) 2021. CC BY 4.0 License.

offset by the shortwave effect. The compensation between longwave and shortwave leads to a net cloud radiative cooling effect in the layers above the cloud top but heating below it. It shifts clear-sky LZRH to higher altitudes, suppressing the diabatic ascents in the TTL.

The cloud radiative heating composited here, particularly the in-cloud heating (below 0.01 $\mathrm{g/m^3}$ IWC contour) and cloud-top cooling feature (above 0.01 $\mathrm{g/m^3}$ IWC contour), corroborates the temperature structure retrieved using the synergistic retrieval method (Fig. 8 (a)). It is also consistent with the finding of Rivoire et al. (2020), who noted a cooling tendency above 100 hPa that is partially attributable to the radiative effect based on an analysis of the COSMIC data.

Figure 11 demonstrates that the cloud radiative heating/cooling changes little with the radial distance. This, however, hides the distinct radiative effects of different types of clouds. For instance, it is well known that thin cirrus absorbs longwave emission from the surface and heats the level it resides (e.g., see Fig. 5 (c) of Rivoire et al. (2020)), although such an effect is not identified anywhere in Fig. 11. Recognizing that clouds types can be differentiated by cloud optical depth and that the window band radiance (BT_{1231}) is sensitive to cloud optical depth over the tropical ocean, we next composite the cloud radiative heating with respect to BT_{1231} to characterize the radiative effects of different types of clouds.

The CloudSat/DARDAR cloud profile is then paired with the nearest AIRS spectra. The AIRS FOVs used are limited to those with scanning angles less than 14 degrees, which has a negligible (<3%) effect on optical depth; the distance between CloudSat sampling location and the center of AIRS FOV is within 6.5 km. A composite of all-sky radiative heating rates, as well as the differences to clear skies, over every 1-K bin of BT_{1231}, are shown in Fig. 12.

Fig. 12 discloses different regimes of cloud radiative effects, which we find are well differentiated by BT_{1231}. When BT_{1231} is colder than 230 K (indicating thick upper tropospheric clouds, as discussed in Section 3), net radiative cooling is observed in TTL, largely caused by longwave cooling above the cloud tops of DCCs (indicated by IWC contours). Note that this BT condition (colder than 230 K) occurs in more than 50 % of the cyclone overpasses within 300 km radius (Fig. 3 (d)), indicating that within this radius TTL is dominated by radiative cooling. In this cloud regime, the cloud effect is to lift the LZRH to higher altitudes, reaching 19.5 km when BT_{1231} is around 200 K. When BT_{1231} is between 240 K and 280 K, noticeable heating near the cloud top emerges (compare Fig. 12 (a) and (b)), attributable to the penetration of solar radiation into the less opaque cloud layer. When BT_{1231} is higher than 294 K (the clear-sky climatological mean value), TTL heating is noticed. This TTL heating is accompanied by a substantial increase of CIs with increasing BT_{1231} as shown in Fig. 12 (f), which suggests the role of thin cirrus in TTL heating as mentioned above.

Furthermore, we compute the net heating anomaly with respect to the all-sky climatology. The all-sky net heating anomaly is then shown as a function of BT_{1231} anomaly, which is defined with respect to the all-sky average, in Fig. 12 (e). It is clear that the cloud effect on the TTL heating rate above 16 km is well-differentiated by BT_{1231}: cooling when BT_{1231} anomaly is negative and heating when BT_{1231} anomaly is positive. Given that negative BT_{1231} anomaly prevails within 1000- km to cyclone center (see the black line in Fig. 3 (d)), no wonder Fig. 11 shows generally TTL cooling above the cyclones.

The prevalence of radiative cooling above tropical cyclones suggests that the diabatic ascent that normally (climatologically) occurs within TTL is suppressed by cloud radiative effects. A hydrated air parcel above a cyclone has to be advected further away from cyclone centers, to be radiatively heated and ascend to the stratosphere.

https://doi.org/10.5194/acp-2021-154
Preprint. Discussion started: 23 April 2021
© Author(s) 2021. CC BY 4.0 License.

Lastly, it is worth noting a few caveats of the cloud radiative effect assessed here. As the cloud radiative effect is measured by the difference in the radiative heating between all- and clear-sky conditions, the result is subject to changes in surface emissions and thermodynamic conditions from the clear-sky to all-sky situations. We cannot quantify how much TTL cooling, as shown in Fig. 12 (d,e), is directly attributable to clouds, because large anomalies in temperature and water vapor, as shown in Fig. 8, exist above the cyclones. It is unclear how much these non-cloud variables account for the radiative heating anomalies shown in Fig. 11 and 12. Moreover, the CloudSat radiative heating data used here may be subject to errors because their calculation is based on the ECMWF forecast which does not fully capture the above-cyclone temperature and water vapor variability (see Fig. 8). It is therefore useful to examine the heating rate change above the cyclones using collocated observations of cloud, temperature, and water vapor profiles from our synergistic retrieval.

4.1 Heating rate decomposition

Large temperature and water vapor anomalies in the TTL above tropical cyclones are detected using the joint AIRS-DARDAR retrieval method, as depicted in Fig. 8. Here, using the radiative transfer model RRTM (Iacono et al., 2000), the radiative effects of the cloud, temperature, and water vapor anomalies are isolated in Fig.13. The shortwave effects of temperature and water vapor are not shown because they are negligible compared to the longwave effects.

Following the idea of Partial Radiative Perturbation (Wetherald and Manabe, 1988), we measure the radiative effect of a variable by differencing the RRTM computations with perturbed and unperturbed values of this variable. For instance, the radiative effect of cyclonic clouds is measured as:

$$dHTR(c) = HTR(c, t0, q0) - HTR(c0, t0, q0) \tag{1}$$

Here, HTR denotes the instantaneous heating rate profile and is computed using RRTM. c, t, and q denote cloud, temperature, and water vapor profiles, respectively, from the cyclone samples. Note that for the t and q profiles, only the portions above 16 km are of concern and replaced in the PRP computation. The variables with subscript 0 denote values from the all-sky climatology. The mean of instantaneous longwave and net radiative heating rate profiles for DCC-OTs, TTL-OTHERs, and NTTLs, are shown in Fig. 13. The radiative effects of temperature and water vapor are examined in both all-sky conditions, denoted by the subscript cld in Fig. 13 (g,h), and clear-sky conditions, denoted by the subscript clr in Fig. 13 (c,d).

By comparing Fig. 13 (a) and (e), we find that the total net radiative effect, $dHTR_{net}(c, t, q)$, is dominated by clouds. The sign and magnitude of the cloud radiative effect are consistent with our previous conclusion, i.e., a cooling effect at the cloud top as indicated by a cold BT_{1231} anomaly (Fig. 12 (a,e)). The cloud longwave cooling effect around 90 hPa is much larger above DCC-OTs due to higher cloud ice water content near this level.

As seen in Fig. 13 (g,h), above 80 hPa where cloud ice diminishes, the all-sky radiative effect of temperature and humidity becomes more important. Temperature modulates the longwave emission to damp the temperature anomalies (compare Fig. 13 (g) to Fig. 9 (c)). For water vapor, a moistening at the cold point increases the thermal emissivity, which leads to cooling at the cold point and heating of lower levels. Therefore, TTL hydration above DCC-OTs and NTTLs leads to radiative cooling in the

https://doi.org/10.5194/acp-2021-154
Preprint. Discussion started: 23 April 2021
© Author(s) 2021. CC BY 4.0 License.

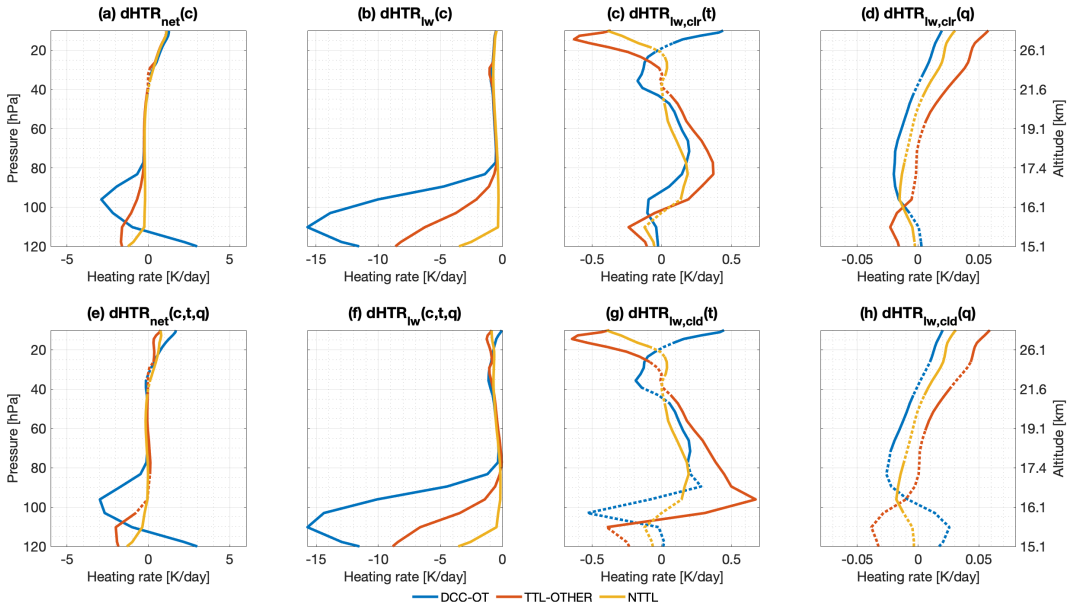

Figure 13. The radiative heating effects of cloud, temperature, and water vapor.

(a) The net effects of cloud, $dHTR_{net}(c)$.

(b) The longwave effects of cloud, $dHTR_{lw}(c)$.

(c) The longwave effects of temperature under clear-sky, $dHTR_{lw,clr}(t)$.

(d) The longwave effects of water vapor under clear-sky, $dHTR_{lw,clr}(q)$.

(e) The net effects of cloud, temperature and water vapor, collectively, $dHTR_{net}(c,t,q)$.

(f) The longwave effects of cloud, temperature, and water vapor, collectively, $dHTR_{lw}(c,t,q)$).

(g) The longwave effects of temperature under cloudy-sky, $dHTR_{lw,cld}(t)$.

(h) The longwave effects of water vapor under cloudy-sky, $dHTR_{lw,cld}(q)$.

TTL. Assuming a similar pattern in thermodynamic anomalies to Fig. 9 (c,d) in the clear-sky, we compute the radiative effects of temperature and water vapor above 80 hPa in the clear-sky (Fig. 13 (c,d)) and find they are similar to all-sky results.

Despite the limited vertical resolution of the water vapor retrieval, as discussed in Appendix A, it is of no ambiguity in that the TTL hydration leads to radiative cooling. It suggests that the moisture above overshooting convections radiatively cools the layer, thus constraining the moist air from diabatically ascending to higher altitudes. This finding is consistent with the robust radiative cooling seen above cyclones in Fig. 12.

https://doi.org/10.5194/acp-2021-154
Preprint. Discussion started: 23 April 2021
© Author(s) 2021. CC BY 4.0 License.

5 Conclusions

In this study, we aim to understand the impacts of tropical cyclones on the thermodynamic conditions in the TTL using multiple instruments aboard the A-Train satellites. We use a TC-overpass product to associate multiple observation products for 947 tropical cyclone center locations over the northern part of the West-Pacific region to ascertain the effect of cyclones. To address the lack of reliable observations of temperature and water vapor when thick convective clouds are present, a retrieval scheme proposed by Feng and Huang (2018) is improved by incorporating cloud properties measured by active sensors to retrieve the above-cyclone temperature and water vapor profile from infrared hyperspectra.

This study finds that tropical cyclones substantially increase TTL clouds. These TTL clouds occur frequently above tropical cyclones, most of which are non-convective high clouds (type CI) (Fig. 3 (b)). This distribution of high clouds is consistent with in-situ aircraft observations (e.g., Jensen et al., 2013). Our finding emphasizes that the occurrence of the TTL cloud is 37.2% on average (Fig. 2 (a) and Fig.3(a)) over the 2000 $\mathrm{km} \times 2000$ km cyclone-centered composite domain, highlighting the importance of tropical cyclone in generating TTL clouds. In contrast to the horizontally extensive occurrence of TTL clouds, the TTL cloud ice is most concentrated near the cyclone center (Fig. 2 (c) and Fig. 3 (a)), as the result of direct overshooting (Fig. 3 (c)). Furthermore, we find the northwest of the composite domain is less impacted by cyclones Fig. 2 (b,j). There is also a persistent southwest preference in TTL cloud ice and DCCs.

The results produced by the synergistic retrieval (Fig.10 (b)) suggest that cyclones mostly hydrate the atmospheric column above them. Above overshooting deep convective clouds, the column-integrated water vapor above 16 km is found to be 40 $\%$ higher than the local climatology (Fig. 10 (b)). Substantial hydration is also found above clouds located beneath 16 km (NTTL). We suspect that this is likely from advected moist plumes from overshooting injection, though we are unable to prove our suspicions at this time. After isolating different cloud categories, dehydration is only found above non-overshooting TTL clouds (TTL-OTHERs) which are coincidently associated with colder temperatures than other cloud categories (Fig. 9 and 10). The coexistence of dehydration (as opposed to the moistening above other cloud categories), cold anomalies, and non-overshooting TTL clouds suggests that in this situation water vapor is likely deposited onto ice particles.

A noticeable pattern of vertically oscillating temperature anomalies, which lifts the cold-point tropopause level to higher altitudes, is found above cyclones. After investigating the cloud radiative effects in Section 4, we find that the signs of the temperature anomaly agree well with cloud radiative heating rates, for example, the in-cloud warming (below 0.01 $\mathrm{g/m^3}$ IWC contour in Fig. 8 (a) and Fig. 12 (d)) due to shortwave heating and the cloud-top cooling due to longwave cooling. The cooling environment may also facilitate the formation of TTL clouds that depletes moisture from the cyclone detrainment, as indicated by the drier TTL over non-overshooting clouds. The cooling effect of cyclones on cold-point temperature also implies the importance of deep convections in modulating the stratospheric water vapor, so that a strong linkage between stratospheric water vapor and cold-point temperature, as noted by Randel and Park (2019), cannot preclude the role of convection in water vapor variability.

By comparing the nearest thermodynamic profiles from the ERA5 (Fig. 8 (c,f)) to the synergistic retrieval (Fig. 8 (a,d)), we find that the cold anomaly in ERA5 is at a lower altitude, which is partially attributable to the biases in cloud ice in the

https://doi.org/10.5194/acp-2021-154
Preprint. Discussion started: 23 April 2021
© Author(s) 2021. CC BY 4.0 License.

reanalysis. The moistening signal around 80 hPa detected by the synergistic retrieval and MLS (Fig. 8 (d,e)) is not shown in ERA5. These results suggest that the above-cyclone water vapor in the reanalysis product may be susceptible to the convective parameterization of the model in simulating cloud ice and temperature (Wright et al., 2020).

Furthermore, we find that the cloud radiative effect is well-differentiated by BT_{1231}. Clouds heat the TTL via radiation when BT_{1231} shows a warm anomaly and cool the TTL when BT_{1231} shows a cold anomaly. Radiative cooling prevails above DCCs and thick anvils which greatly reduce BT_{1231}. Radiative warming becomes more noticeable away from the cyclone center over thin cirrus. The radiative cooling anomaly further impacts the diabatic heating budget above the cyclones, thus suppressing the diabatic ascent and transportation of air masses to higher altitudes. It remains unclear how the suppressed diabatic ascent, together with the strong horizontal divergence created by the pressure gradient above the cyclone, can affect the stratosphere-tropopause exchange and the water vapor budget. To elucidate this effect in the trajectory modeling in future work, it will require the use of instantaneous radiative heating computed from deep convection-perturbed TTL thermodynamic conditions (temperature, humidity and cloud), as opposed to climatologic or reanalysis heating profiles that do not properly represent the convective perturbations.

Finally, we would like to highlight the advantages of the synergistic method in retrieving the above-cloud conditions. This method takes advantage of collocated infrared hyperspectra and active sensors and is capable of retrieving temperature and water vapor under overcast cloud conditions, which is highly complementary to other datasets, including MLS v4.2 and AIRS L2 v6, that are limited to the clear-sky condition. So far, this approach is only applied to limited samples in the vicinity of tropical cyclones. It can be applied to other tropical and extra-tropical convective events, with potential implementation in other hyperspectral infrared sounders, e.g, IASI (Infrared Atmospheric Sounding Interferometer), CrIS (Cross-track Infrared Sounder), IRS (Infrared Spectrometer), and GIIRS (Geostationary Interferometric Infrared Sounder), to provide thermodynamic information over deep convective clouds on a global scale in future research.

Author contributions. YH conceived the cloud-assisted retrieval idea; JF implemented this idea with improvements using A-Train measurements. JF and YH co-designed the study of the tropical cyclone impacts and collectively wrote this paper.

Competing interests. The authors declare that they have no conflict of interest.

Acknowledgements. We thank Xun Wang, Kevin Bloxam, Lei Liu, and two anonymous reviewers for their constructive comments. This work is supported by grants from the Canadian Space Agency (16SUASURDC and 21SUASATHC) and the Natural Sciences and Engineering Research Council of Canada (RGPIN-2019-04511). JF acknowledges the support of a Milton Leong Graduate Fellowship of McGill University. We thank Natalie Tourville for making the TC overpass dataset publically accessible (https://adelaide.cira.colostate.edu/tc/). We thank ICARE Data and Services Center (http://www.icare-lille1.fr) and Dr. Julien Delanoë for access to the DARDAR product.

https://doi.org/10.5194/acp-2021-154
Preprint. Discussion started: 23 April 2021
© Author(s) 2021. CC BY 4.0 License.

Appendix A: Joint AIRS-DARDAR retrieval algorithm

Feng and Huang (2018) applied a cloud-assisted retrieval to AIRS L1B infrared radiance from FOVs filled with deep convective clouds, assuming a blackbody cloud top. This method retrieves the atmospheric temperature and humidity above the cloud top as described in Section 2.1 and it can especially take advantage of overcast conditions during tropical cyclone events. An updated version of this retrieval method is validated by Feng et al. (2021) via simulation experiments and is adopted here. We briefly describe this retrieval method below and interested readers can find more details of this retrieval method from Feng et al. (2021).

In this method, we retrieve atmospheric states x that includes temperature, humidity, and ice water content (IWC) as an optimal estimation (Rodgers, 2000) that combines the $a\ priori$ of x and the observation vector, y. The relationship between the state vector and the observation vector is expressed as:

$$\begin{aligned} y &= F(x_0) + \frac{\partial F}{\partial x}(x - x_0) + \varepsilon \\ &= y_0 + K(x - x_0) + \varepsilon \end{aligned} \tag{A1}$$

Where F is the forward model, K is the jacobian matrix, which is a first-order linear approximation of F, and ε is the residual. x_0 is the first guess, for which we use the mean of the $a\ priori$. Following the synergistic retrieval method (Feng et al., 2021), additional observation vectors are added, so that y is formed as [y_{rad},y_{iwc},y_{atm}]. y_{rad} is the infrared hyperspectra from AIRS L1B product, for which 1109 channels are selected, based on the radiometric quality of each channel. This rigorous channel selection also excludes O3 absorption channels (980-1140 cm^{-1}), CH4 absorption channels (1255-1355 cm^{-1}), and shortwave infrared channels (2400-2800 cm^{-1}). y_{iwc} is a 2-km vertical IWC profile from DARDAR-Cloud product, from 1.5 km below the DARDAR-identified cloud top to 0.5 km above it, and y_{atm} is the temperature and humidity profile from the nearest ERA5 reanalysis product (hourly, 0.25 × 0.25). The $a\ priori$ dataset is obtained from AIRS L2 v6 supplementary product from 2006 to 2016 in the Northern part of the West Pacific.

The forward model to convert the atmospheric states to y_{rad} is a radiative transfer model, the line-by-line version of MODerate spectral resolution TRANsmittance (MODTRAN 6.0 Berk et al., 2014). To relate x to y_{iwc} and y_{atm}, the forward model and the corresponding Jacobian matrix work as a linear interpolation matrix (Turner and Blumberg, 2018; Feng et al., 2021).

Using the Gaussian-Newton method, the best estimate of x, $\hat{x}$, is iteratively solved as:

$$\begin{aligned} \hat{x}_{i+1} &= x_0 + (K_i^T S_\varepsilon^{-1} K_i + S_a^{-1})^{-1} K_i^T S_\varepsilon^{-1} [y - F(\hat{x}_i) + K_i(\hat{x}_i - x_0)] \\ \hat{x}_{i+1} &= x_0 + (K_i^T S_\varepsilon^{-1} K_i + S_a^{-1})^{-1} K_i^T S_\varepsilon^{-1} [y - F(\hat{x}_i)] + A(\hat{x}_i - x_0) \end{aligned} \tag{A2}$$

Where the subscript i refers to the ith time step. S_a and S_ε are the covariance matrix of the $a\ priori$ dataset and the observation vector, respectively, which are constructed the same as in Feng et al. (2021). More specifically, the S_ε for y_{iwc} is a diagonal matrix, containing the square of the posterior uncertainty of the IWC profile which is provided by the DARDAR-Cloud product at every measurement location and vertical level. The S_ε for y_{atm} is denoted as S_{atm}; it contains the square of a doubling of the root-mean-square difference between collocated ERA5 and MLS v4.2 product at every vertical level of ERA5.

https://doi.org/10.5194/acp-2021-154
Preprint. Discussion started: 23 April 2021
© Author(s) 2021. CC BY 4.0 License.

The A in Eq. A2 is referred to as averaging kernel. Given a 'truth' state vector that $F(x_t) = y$, it links the truth state to the retrieved state, so that:

$$\hat{x} - x_0 = A(x_t - x_0). \tag{A3}$$

Therefore, it regulates the vertical shape of the posterior estimation.

The iteration converges when:

$$(\hat{x}_{i+1} - \hat{x}_i)^T S(\hat{x}_{i+1} - \hat{x}_i) \ll N, \tag{A4}$$

where N is the dimension of the state vector, and S is the posterior covariance matrix, which is computed combining the covariance matrix of $a\ priori$ and observation vector:

$$S = (S_a^{-1} + K^T S_\varepsilon^{-1} K)^{-1} \tag{A5}$$

Therefore, the uncertainty in the $\hat{x}$ is equivalent to the square root of the diagonal element of the posterior covariance matrix S.

Feng et al. (2021) used a system simulation experiment to evaluate a synergistic retrieval approach that combines infrared spectra (y_{rad}) with another observation vector that includes IWC product from collocated observation vector, denoted as y_{iwc}, and additional atmospheric observations, denoted as y_{atm}. In this simulation experiment, the 'truth' atmospheric condition is simulated from a cloud-resolving model during a tropical cyclone event. We mimic the infrared spectra from AIRS observation by adding synthetic noise to the forward model simulated infrared radiances that follow the spectral response function of AIRS. The IWC observation is simulated by perturbing the 'truth' IWC profile following the mean posterior uncertainty range provided by the DARDAR-Cloud product within 1000 km from cyclone centers. Therefore, the simulation experiment is designed to evaluate the realistic retrieval performance above thick upper-tropospheric clouds using AIRS L1B and DARDAR-Cloud product, with the same S_ε for the observation vectors.

The synergistic retrieval performed here is similar to Case 4 in Feng et al. (2021); the only differences are in the $a\ priori$ dataset and the y_{atm}, which Feng et al. (2021) constructed hypothetically using numerical model simulation. To examine the capacity of the retrieval method in revealing the realistic thermodynamic conditions, a simulation experiment similar to Feng et al. (2021) is performed here, using the $a\ priori$ dataset and S_ε we introduced earlier. Figure A1 shows the horizontal distribution of temperature and water vapor at 81 hPa, as well as the column-integrated water vapor (CIWV, between 100 to 70 hPa) from the simulated 'truth', the prior, the nearest ERA5 (y_{atm}), and the posterior of the retrieval. In Figure A1, the posterior shows a noticeable improvement compared to the prior and y_{atm} in reducing the mean biases and root-mean-square-error (RMSE). As a result, the posterior reveals the spatial feature of the 'truth', namely a moister and colder cyclone center.

According to Eq. A4 and A5, the precision of this synergistic retrieval algorithm is given by the posterior uncertainty S, which is shown in Figure A2. The posterior uncertainty is within 1 K in temperature and is around 0.5 ppmv in water vapor around 80 hPa. While the uncertainty in IWC is equivalent to the DARDAR-Cloud product, the simulation experiment

https://doi.org/10.5194/acp-2021-154
Preprint. Discussion started: 23 April 2021
© Author(s) 2021. CC BY 4.0 License.

conducted by Feng et al. (2021) showed that the retrieval can reduce the mean biases and RMSE in collocated IWC products caused by issues such as footprint mismatch.

Compared to other current satellite observational products in the UTLS, this retrieval has several advantages. First, the relatively small sampling footprint (15 km, the same as the size of the AIRS instantaneous FOV in the nadir) compared to limb-viewing sounders (>100 km) is beneficial for capturing small-scale variability directly impacted by deep convections. Second, the ability to retrieve temperature and water vapor above storms simultaneously. Third, the ability to retrieve atmospheric profiles near the cloud top. The simulation experiment conducted by Feng et al. (2021) evidenced that the synergistic method is capable of sounding the temperature profile near and slightly below the cloud top (within cloud optical depth of 1), while other products may not perform all-sky retrieval (AIRS L2, Susskind et al., 2003) or may be degraded by cloud presence (MLS v4.2 Schwartz et al., 2008; Livesey et al., 2017).

As depicted in the simulation experiment, the synergistic retrieval reveals the spatial variation in temperature and humidity. The retrieval is sensitive to the vertical variation of temperature (Fig. A3 (a,b)) but is not as sensitive to the vertical variation of water vapor (Fig. A3 (c,d)). The coarse resolution of the water vapor retrieval is due to the smearing effect of the averaging kernel (Feng et al., 2021). This smearing effect is illustrated in Fig. A3. In this test, we increase the temperature at every 20 hPa interval by 5 K as shown in Fig. A3 (a), this corresponds to the term $x_t - x_0$ in Eq. A3. Similarly, the water vapor mixing ratio at every 20 hPa interval is increased by 50 $\%$ (considering the water vapor radiative effect is logarithmically scaled), as shown in Fig. A3 (c). The responses from the averaging kernel are then calculated using Eq. A3, which are shown in Fig. A3 (b,d) for temperature and water vapor, respectively. Figure A3 (a,b) shows that the retrieved temperature responds well to perturbation at different vertical ranges. However, Fig. A3 (c,d) shows that the fine-scale water vapor perturbation would result in vertically broad, bottom-heavy water vapor anomalies in the retrieval. Nevertheless, the retrieval determines the changes in CIWV properly to detect (de)hydration. This is verified by the tests illustrated in Fig. A3 (c). Here, we prescribe random hydrations or dehydrations in randomly selected 20 hPa thick layers between 20 to 100 hPa, following the same pattern in Fig. A3(c), for 1000 cases. We find that the CIWV changes produced by averaging kernel approach the truth better at higher altitudes, suggesting that the retrieval is more sensitive to perturbations at higher altitudes.

To evaluate the effects of cyclones on water vapor, samples above cyclones are compared to the climatology computed from the multi-year monthly mean of MLS data at the same grid as the retrieval samples. To remove the systematic bias caused by the higher vertical resolution of the MLS product, the MLS climatology is converted to the same vertical resolution using the averaging kernel of the synergistic retrieval, following Equation A3. The mean of the converted climatology profiles at retrieved sample locations is shown in Fig. 9 (b) black line, while the mean of retrieved water vapor anomalies in comparison with this converted climatology is shown in Fig. 8 (d) and Fig. 9 (d). These anomalies measure the impacts of cyclones. We note that this bias correction procedure affects the vertical structure of anomaly in water vapor, but has a negligible impact on the anomaly in CIWV. Therefore, the conclusion on the hydration and dehydration impacts as shown in Fig. 10 are robust.

https://doi.org/10.5194/acp-2021-154
Preprint. Discussion started: 23 April 2021
© Author(s) 2021. CC BY 4.0 License.

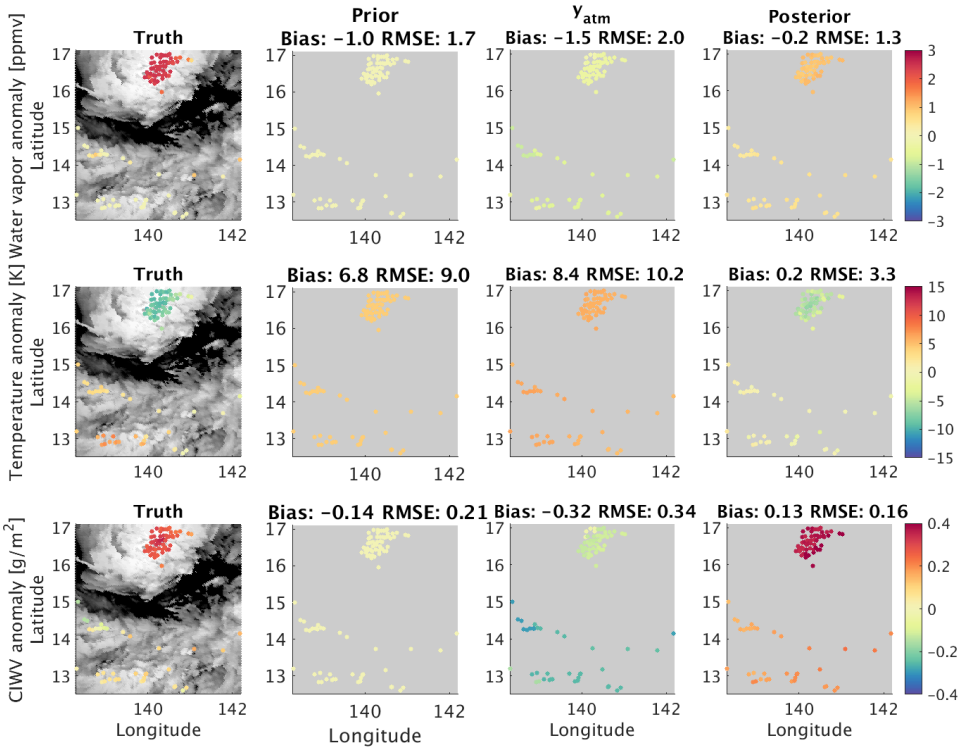

Figure A1. Horizontal distributions of the anomalies, defined as the deviation from the all-sky mean of the simulation field, in water vapor (in the units of ppmv, upper panels), temperature (in the units of K, middle panels) at 81 hPa, and column integrated water vapor between 110 and 70 hPa (in the units of g/m^2, lower panels). The truth fields are shown in the first column, with its background grey-shaded for BT_{1231}. The other columns show the distribution in the prior, nearest ERA5 (y_{atm}), and the posterior of the retrieval.

Appendix B: Binary classification of overshooting deep convective clouds

Similar to previous studies (Aumann and Ruzmaikin, 2013), we investigate BT of window channel at wavenumber 1231 cm^{-1} (BT_{1231}) and water vapor absorption channel at wavenumber 1419 cm^{-1} (BT_{1419}). In this section, we use collocated AIRS radiances observation and DARDAR IWC product to evaluate the two metrics quantitatively and to identify the best threshold for determining the DCC-OTs.

As shown in Fig. B1, the distributions of BT_{1231} and ΔBT of overshooting DCCs resemble the Gaussian distribution in the intervals of [210 185] K and [-2 12] K, respectively. To find the optimized threshold for DCC-OT classification, we calculate the accuracy and the f1 score of DCC-OT classification combining $BT_{1231} <= \varepsilon_{BT}$ and $\Delta BT >= \varepsilon_{\Delta BT}$. The accuracy ($\alpha$)

https://doi.org/10.5194/acp-2021-154
Preprint. Discussion started: 23 April 2021
© Author(s) 2021. CC BY 4.0 License.

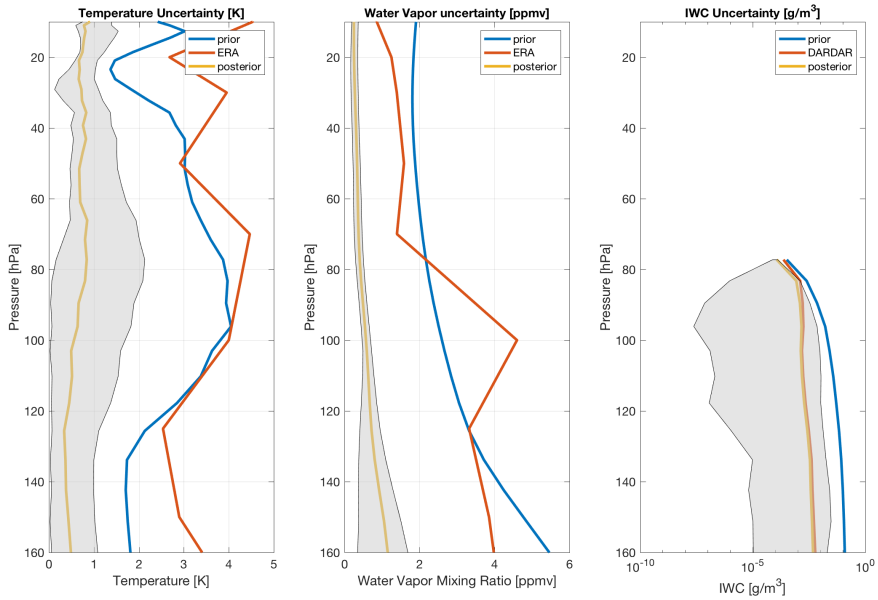

Figure A2. Uncertainties in temperature, water vapor mixing ratio, and IWC, estimated from the average of 2735 retrieved profiles with varied cloud top heights. Blue, red, and yellow curves show uncertainties of the prior (S_a), the ERA5 (S_{model}), and the posterior (S_{post}), respectively. The grey shaded area is the range of posterior uncertainties.

and the f1 score ($F1$) are defined as:

$$\alpha = \frac{TP+TN}{TP+FP+FN+TN};$$
$$P = \frac{TP}{TP+FP};$$
$$R = \frac{TP}{TP+FN};$$
$$F1 = 2 \times \frac{R \times P}{R+P}; \tag{B1}$$

Where the TP, TN, FP, and FN is the number of true positive, true negative, false positive, and false negative, respectively. While the P and R represent the precision and recall (equivalent with true positive rate) of this classification, the f1 score considers both by a harmonic average of the two factors.

As indicated by Fig. B1 (c), the accuracy of the classification gets around 0.985 when $\varepsilon_{BT} <= 204$ K or $\varepsilon_{\Delta BT} >= 2$ K. However, this high accuracy is partly a result of a small sample size from DCC-OT compared to the total. The f1 score is therefore used instead. The maximum $F1$ appears when $\varepsilon_{BT} = 203$ K and $\varepsilon_{\Delta BT} = 1$ K, although adding $\varepsilon_{\Delta BT}$ criterion only increase $F1$ by 0.0004 which is considered to be negligible here. Using $\varepsilon_{BT} = 203$ K leads to an FP rate at 0.008 and an FN rate at 0.323. Fig. B1 (b) shows that the FP mainly comes from MIX and CI; their cold brightness temperature signal indicates sources from thick anvil cloud near the edge of the DCC system.

https://doi.org/10.5194/acp-2021-154
Preprint. Discussion started: 23 April 2021
© Author(s) 2021. CC BY 4.0 License.

Atmospheric Chemistry and Physics Discussions

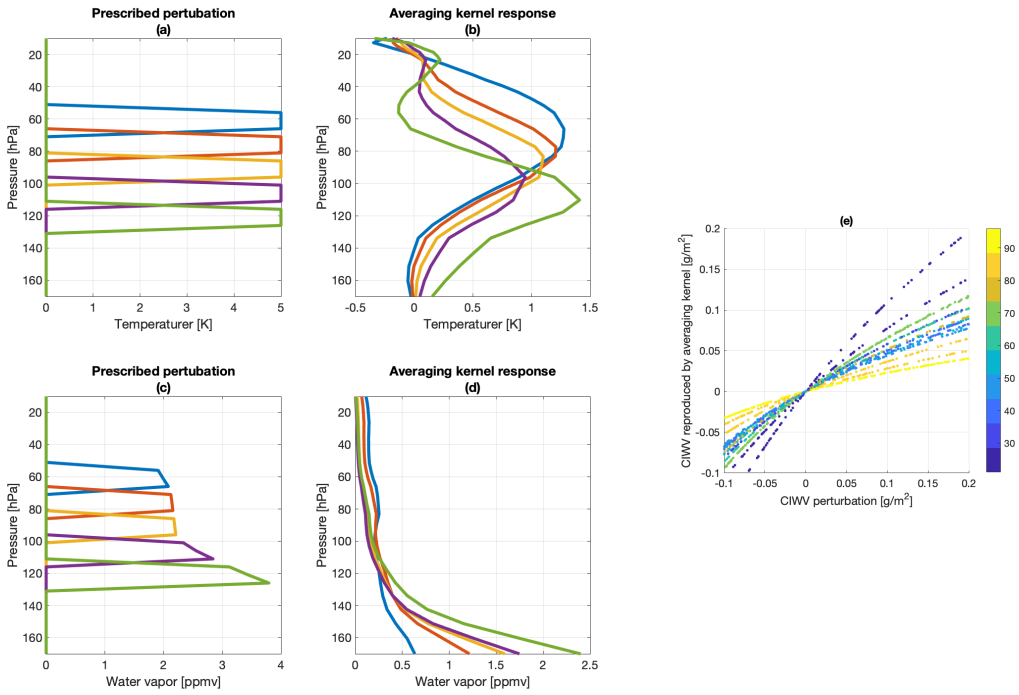

Figure A3. Averaging kernel responses to temperature and water vapor perturbation in thin layers. (a) Prescribed perturbation and (b) the response of averaging kernel in temperature [K]. (c) Prescribed perturbation and (d) the response of averaging kernel in water vapor [ppmv]. (e) CIWV perturbation [g/m^2] between 100 to 20 hPa reproduced by averaging kernel, color-coded for vertical pressure intervals (hPa) where the perturbation is prescribed.

https://doi.org/10.5194/acp-2021-154
Preprint. Discussion started: 23 April 2021
© Author(s) 2021. CC BY 4.0 License.

Atmospheric Chemistry and Physics Discussions
Open Access

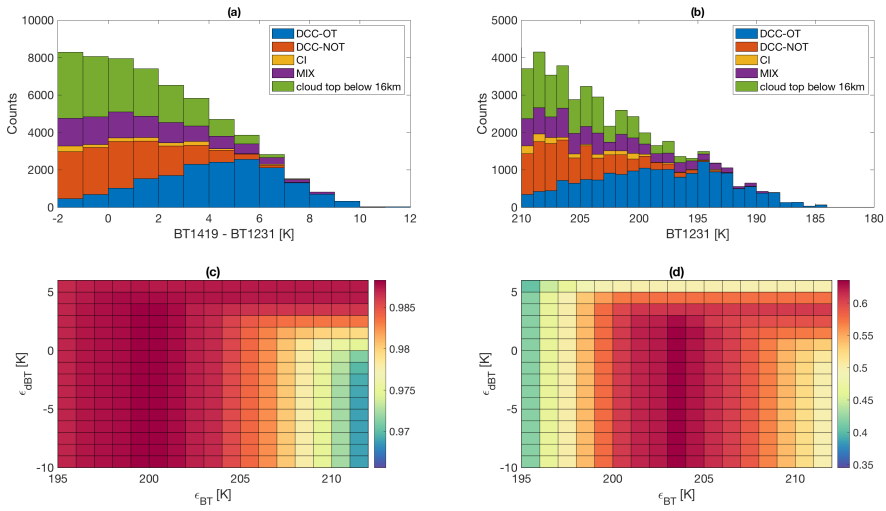

Figure B1. Distribution of (a) BT_{1419}-BT_{1231} and (b) BT_{1231} of AIRS FOVs under four TTL cloud categories and NTTLs (cloud top below 16 km). (c) The accuracy (Eq.1, α) and (d) f1 score ($F1$) of the DCC-OT classification using $BT_{1231} <= \varepsilon_{BT}$ and BT_{1419}-$BT_{1231} >= \varepsilon_{\Delta BT}$ criterion.

https://doi.org/10.5194/acp-2021-154
Preprint. Discussion started: 23 April 2021
© Author(s) 2021. CC BY 4.0 License.

References

Anderson, J. G., Wilmouth, D. M., Smith, J. B., and Sayres, D. S.: UV dosage levels in summer: Increased risk of ozone loss from convectively injected water vapor, Science, 337, 835–839, 2012.

Anthes, R. A., Bernhardt, P., Chen, Y., Cucurull, L., Dymond, K., Ector, D., Healy, S., Ho, S.-P., Hunt, D., Kuo, Y.-H., et al.: The COSMIC/FORMOSAT-3 mission: Early results, Bulletin of the American Meteorological Society, 89, 313–334, 2008.

Aumann, H. and Ruzmaikin, A.: Frequency of deep convective clouds in the tropical zone from 10 years of AIRS data, Atmospheric Chemistry and Physics, 13, 10 795, 2013.

Aumann, H., DeSouza-Machado, S., and Behrangi, A.: Deep convective clouds at the tropopause, Atmospheric Chemistry and Physics, 11, 1167, 2011.

Avery, M. A., Davis, S. M., Rosenlof, K. H., Ye, H., and Dessler, A. E.: Large anomalies in lower stratospheric water vapour and ice during the 2015–2016 El Niño, Nature Geoscience, 10, 405–409, 2017.

Berk, A., Conforti, P., Kennett, R., Perkins, T., Hawes, F., and Van Den Bosch, J.: MODTRAN® 6: A major upgrade of the MODTRAN® radiative transfer code, in: 2014 6th Workshop on Hyperspectral Image and Signal Processing: Evolution in Remote Sensing (WHISPERS), pp. 1–4, IEEE, 2014.

Bernath, P. F., McElroy, C. T., Abrams, M., Boone, C. D., Butler, M., Camy-Peyret, C., Carleer, M., Clerbaux, C., Coheur, P.-F., Colin, R., et al.: Atmospheric chemistry experiment (ACE): mission overview, Geophysical Research Letters, 32, 2005.

Biondi, R., Ho, S.-P., Randel, W., Syndergaard, S., and Neubert, T.: Tropical cyclone cloud-top height and vertical temperature structure detection using GPS radio occultation measurements, Journal of Geophysical Research: Atmospheres, 118, 5247–5259, 2013.

Brewer, A.: Evidence for a world circulation provided by the measurements of helium and water vapour distribution in the stratosphere, Quarterly Journal of the Royal Meteorological Society, 75, 351–363, 1949.

Chahine, M. T., Pagano, T. S., Aumann, H. H., Atlas, R., et al.: AIRS: Improving weather forecasting and providing new data on greenhouse gases, Bulletin of the American Meteorological Society, 87, 911, 2006.

Delanoë, J. and Hogan, R. J.: A variational scheme for retrieving ice cloud properties from combined radar, lidar, and infrared radiometer, Journal of Geophysical Research: Atmospheres, 113, 2008.

Delanoë, J. and Hogan, R. J.: Combined CloudSat-CALIPSO-MODIS retrievals of the properties of ice clouds, Journal of Geophysical Research: Atmospheres, 115, 2010.

Dessler, A., Hintsa, E., Weinstock, E., Anderson, J., and Chan, K.: Mechanisms controlling water vapor in the lower stratosphere:"A tale of two stratospheres", Journal of Geophysical Research: Atmospheres, 100, 23 167–23 172, 1995.

Dessler, A., Schoeberl, M., Wang, T., Davis, S., and Rosenlof, K.: Stratospheric water vapor feedback, Proceedings of the National Academy of Sciences, 110, 18 087–18 091, 2013.

Feng, J. and Huang, Y.: Cloud-Assisted Retrieval of Lower-Stratospheric Water Vapor from Nadir-View Satellite Measurements, Journal of Atmospheric and Oceanic Technology, 35, 541–553, 2018.

Feng, J., Huang, Y., and Qu, Z.: A simulation experiment-based assessment of the retrieval of above-cloud temperature and water vapor using infrared hyper-spectrometers, Manuscript submitted for publication, https://doi.org/10.5194/amt-2020-518, 2021.

Fetzer, E. J., Read, W. G., Waliser, D., Kahn, B. H., Tian, B., Vömel, H., Irion, F. W., Su, H., Eldering, A., de la Torre Juarez, M., Jiang, J., and Dang, V.: Comparison of upper tropospheric water vapor observations from the Microwave Limb Sounder and Atmospheric Infrared

https://doi.org/10.5194/acp-2021-154
Preprint. Discussion started: 23 April 2021
© Author(s) 2021. CC BY 4.0 License.

Sounder, Journal of Geophysical Research: Atmospheres, 113, n/a–n/a, https://doi.org/10.1029/2008JD010000, http://dx.doi.org/10.1029/2008JD010000, d22110, 2008.

Gettelman, A., Randel, W., Wu, F., and Massie, S.: Transport of water vapor in the tropical tropopause layer, Geophysical research letters, 29, 9–1, 2002.

Gettelman, A., Weinstock, E. M., Fetzer, E. J., Irion, F. W., Eldering, A., Richard, E. C., Rosenlof, K. H., Thompson, T. L., Pittman, J. V., Webster, C. R., and Herman, R. L.: Validation of Aqua satellite data in the upper troposphere and lower stratosphere with in situ aircraft instruments, Geophysical Research Letters, 31, n/a–n/a, https://doi.org/10.1029/2004GL020730, http://dx.doi.org/10.1029/2004GL020730, l22107, 2004.

Hersbach, H., Bell, B., Berrisford, P., Hirahara, S., Horányi, A., Muñoz-Sabater, J., Nicolas, J., Peubey, C., Radu, R., Schepers, D., et al.: The ERA5 global reanalysis, Quarterly Journal of the Royal Meteorological Society, 146, 1999–2049, 2020.

Holloway, C. E. and Neelin, J. D.: The convective cold top and quasi equilibrium, Journal of the atmospheric sciences, 64, 1467–1487, 2007.

Holton, J. R. and Gettelman, A.: Horizontal transport and the dehydration of the stratosphere, Geophysical Research Letters, 28, 2799–2802, 2001.

Holton, J. R., Haynes, P. H., McIntyre, M. E., Douglass, A. R., Rood, R. B., and Pfister, L.: Stratosphere-troposphere exchange, Reviews of geophysics, 33, 403–439, 1995.

Huang, Y., Ramaswamy, V., Huang, X., Fu, Q., and Bardeen, C.: A strict test in climate modeling with spectrally resolved radiances: GCM simulation versus AIRS observations, Geophysical Research Letters, 34, 2007.

Huang, Y., Zhang, M., Xia, Y., Hu, Y., and Son, S.-W.: Is there a stratospheric radiative feedback in global warming simulations?, Climate dynamics, 46, 177–186, 2016.

Iacono, M. J., Mlawer, E. J., Clough, S. A., and Morcrette, J.-J.: Impact of an improved longwave radiation model, RRTM, on the energy budget and thermodynamic properties of the NCAR community climate model, CCM3, Journal of Geophysical Research: Atmospheres, 105, 14 873–14 890, 2000.

Jensen, E., Ackerman, A., and Smith, J.: Can overshooting convection dehydrate the tropical tropopause layer?, Journal of Geophysical Research: Atmospheres, 112, 2007.

Jensen, E. J., Pfister, L., Jordan, D. E., Fahey, D. W., Newman, P. A., Thornberry, T., Rollins, A., Diskin, G., Bui, T. P., McGill, M., et al.: The NASA Airborne Tropical TRopopause EXperiment (ATTREX), SPARC Newsletter, 41, 15–24, 2013.

Jiang, J. H., Su, H., Zhai, C., Perun, V. S., Del Genio, A., Nazarenko, L. S., Donner, L. J., Horowitz, L., Seman, C., Cole, J., et al.: Evaluation of cloud and water vapor simulations in CMIP5 climate models using NASA "A-Train" satellite observations, Journal of Geophysical Research: Atmospheres, 117, 2012.

Jiang, J. H., Su, H., Zhai, C., Wu, L., Minschwaner, K., Molod, A. M., and Tompkins, A. M.: An assessment of upper troposphere and lower stratosphere water vapor in MERRA, MERRA2, and ECMWF reanalyses using Aura MLS observations, Journal of Geophysical Research: Atmospheres, 120, 11–468, 2015.

L'Ecuyer, T. S. and Jiang, J. H.: Touring the atmosphere aboard the A-Train, in: AIP Conference Proceedings, vol. 1401, pp. 245–256, American Institute of Physics, 2011.

Lee, K.-O., Dauhut, T., Chaboureau, J.-P., Khaykin, S., Krämer, M., and Rolf, C.: Convective hydration in the tropical tropopause layer during the StratoClim aircraft campaign: pathway of an observed hydration patch, 2019.

Livesey, N., Read, W., Wagner, P., Froidevaux, L., Lambert, A., Manney, G., Millán Valle, L., Pumphrey, H., Santee, M., Schwartz, M., et al.: Version 4.2 x Level 2 data quality and description document, JPL D-33509 Rev. C, 2017.

https://doi.org/10.5194/acp-2021-154
Preprint. Discussion started: 23 April 2021
© Author(s) 2021. CC BY 4.0 License.

L'Ecuyer, T.: Level 2 fluxes and heating rates product process description and interface control document, v. 5, 2007.

Olsen, E., Fetzer, E., Hulley, G., Manning, E., Blaisdell, J., Iredell, L., Susskind, J., Warner, J., Wei, Z., Blackwell, W., et al.: AIRS/AMSU/HSB version 6 level 2 product user guide, Jet Propulsion Laboratory, Version, 1, 2013.

Parkinson, C. L.: Aqua: An Earth-observing satellite mission to examine water and other climate variables, IEEE Transactions on Geoscience and Remote Sensing, 41, 173–183, 2003.

Partain, P.: Cloudsat ECMWF-AUX auxiliary data process description and interface control document, Cooperative Institute for Research in the Atmosphere Rep, 2004.

Qu, Z., Huang, Y., Vaillancourt, P. A., Cole, J. N., Milbrandt, J. A., Yau, M.-K., Walker, K., and de Grandpré, J.: Simulation of convective moistening of the extratropical lower stratosphere using a numerical weather prediction model., Atmospheric Chemistry & Physics, 20, 2020.

Randel, W. and Park, M.: Diagnosing observed stratospheric water vapor relationships to the cold point tropical tropopause, Journal of Geophysical Research: Atmospheres, 124, 7018–7033, 2019.

Read, W. G., Lambert, A., Bacmeister, J., Cofield, R. E., Christensen, L. E., Cuddy, D. T., Daffer, W. H., Drouin, B. J., Fetzer, E., Froidevaux, L., Fuller, R., Herman, R., Jarnot, R. F., Jiang, J. H., Jiang, Y. B., Kelly, K., Knosp, B. W., Kovalenko, L. J., Livesey, N. J., Liu, H.-C., Manney, G. L., Pickett, H. M., Pumphrey, H. C., Rosenlof, K. H., Sabounchi, X., Santee, M. L., Schwartz, M. J., Snyder, W. V., Stek, P. C., Su, H., Takacs, L. L., Thurstans, R. P., Vömel, H., Wagner, P. A., Waters, J. W., Webster, C. R., Weinstock, E. M., and Wu, D. L.: Aura Microwave Limb Sounder upper tropospheric and lower stratospheric H2O and relative humidity with respect to ice validation, Journal of Geophysical Research: Atmospheres, 112, n/a–n/a, https://doi.org/10.1029/2007JD008752, http://dx.doi.org/10.1029/2007JD008752, d24S35, 2007.

Rivoire, L., Birner, T., and Knaff, J. A.: Evolution of the upper-level thermal structure in tropical cyclones, Geophysical Research Letters, 43, 10–530, 2016.

Rivoire, L., Birner, T., Knaff, J. A., and Tourville, N.: Quantifying the radiative impact of clouds on tropopause layer cooling in tropical cyclones, Journal of Climate, 2020.

Robinson, F. and Sherwood, S.: Modeling the impact of convective entrainment on the tropical tropopause, Journal of the atmospheric sciences, 63, 1013–1027, 2006.

Rodgers, C. D.: Inverse methods for atmospheric sounding: theory and practice, vol. 2, World scientific, 2000.

Romps, D. M. and Kuang, Z.: Overshooting convection in tropical cyclones, Geophysical Research Letters, 36, 2009.

Sampson, C. R. and Schrader, A. J.: The automated tropical cyclone forecasting system (version 3.2), Bulletin of the American Meteorological Society, 81, 1231–1240, 2000.

Schoeberl, M. R., Jensen, E. J., Pfister, L., Ueyama, R., Avery, M., and Dessler, A. E.: Convective hydration of the upper troposphere and lower stratosphere, Journal of Geophysical Research: Atmospheres, 123, 4583–4593, 2018.

Schubert, W. H. and McNoldy, B. D.: Application of the concepts of Rossby length and Rossby depth to tropical cyclone dynamics, Journal of Advances in Modeling Earth Systems, 2, 2010.

Schwartz, M., Lambert, A., Manney, G., Read, W., Livesey, N., Froidevaux, L., Ao, C., Bernath, P., Boone, C., Cofield, R., et al.: Validation of the Aura Microwave Limb Sounder temperature and geopotential height measurements, Journal of Geophysical Research: Atmospheres, 113, 2008.

Schwartz, M. J., Read, W. G., Santee, M. L., Livesey, N. J., Froidevaux, L., Lambert, A., and Manney, G. L.: Convectively injected water vapor in the North American summer lowermost stratosphere, Geophysical Research Letters, 40, 2316–2321, 2013.

https://doi.org/10.5194/acp-2021-154
Preprint. Discussion started: 23 April 2021
© Author(s) 2021. CC BY 4.0 License.

Solomon, S., Rosenlof, K. H., Portmann, R. W., Daniel, J. S., Davis, S. M., Sanford, T. J., and Plattner, G.-K.: Contributions of stratospheric water vapor to decadal changes in the rate of global warming, Science, 327, 1219–1223, 2010.

Stephens, G. L., Vane, D. G., Tanelli, S., Im, E., Durden, S., Rokey, M., Reinke, D., Partain, P., Mace, G. G., Austin, R., et al.: CloudSat mission: Performance and early science after the first year of operation, Journal of Geophysical Research: Atmospheres, 113, 2008.

Sun, Y. and Huang, Y.: An examination of convective moistening of the lower stratosphere using satellite data, Earth and Space Science, 2, 320–330, 2015.

Susskind, J., Barnet, C. D., and Blaisdell, J. M.: Retrieval of atmospheric and surface parameters from AIRS/AMSU/HSB data in the presence of clouds, IEEE Transactions on Geoscience and Remote Sensing, 41, 390–409, 2003.

Takahashi, H., Su, H., and Jiang, J. H.: Error analysis of upper tropospheric water vapor in CMIP5 models using "A-Train" satellite observations and reanalysis data, Climate dynamics, 46, 2787–2803, 2016.

Tourville, N., Stephens, G., DeMaria, M., and Vane, D.: Remote sensing of tropical cyclones: Observations from CloudSat and A-Train profilers, Bulletin of the American Meteorological Society, 96, 609–622, 2015.

Turner, D. D. and Blumberg, W. G.: Improvements to the AERIoe thermodynamic profile retrieval algorithm, IEEE Journal of Selected Topics in Applied Earth Observations and Remote Sensing, 12, 1339–1354, 2018.

Ueyama, R., Jensen, E. J., and Pfister, L.: Convective influence on the humidity and clouds in the tropical tropopause layer during boreal summer, Journal of Geophysical Research: Atmospheres, 123, 7576–7593, 2018.

Wang, Z. and Sassen, K.: Level 2 cloud scenario classification product process description and interface control document, Coop. Inst. for Res. in the Atmos, 2007.

Waters, J. W., Froidevaux, L., Harwood, R. S., Jarnot, R. F., Pickett, H. M., Read, W. G., Siegel, P. H., Cofield, R. E., Filipiak, M. J., Flower, D. A., et al.: The earth observing system microwave limb sounder (EOS MLS) on the Aura satellite, IEEE Transactions on Geoscience and Remote Sensing, 44, 1075–1092, 2006.

Wetherald, R. and Manabe, S.: Cloud feedback processes in a general circulation model, Journal of Atmospheric Sciences, 45, 1397–1416, 1988.

Winker, D., Pelon, J., Coakley Jr, J., Ackerman, S., Charlson, R., Colarco, P., Flamant, P., Fu, Q., Hoff, R., Kittaka, C., et al.: The CALIPSO mission: A global 3D view of aerosols and clouds, Bulletin of the American Meteorological Society, 91, 1211–1230, 2010.

WMO, W. M. O.: Definition of the tropopause, WMO Bull., 6, 136, 1957.

Wright, J. and Fueglistaler, S.: Large differences in reanalyses of diabatic heating in the tropical upper troposphere and lower stratosphere., Atmospheric Chemistry & Physics, 13, 2013.

Wright, J. S., Sun, X., Konopka, P., Krüger, K., Molod, A. M., Tegtmeier, S., Zhang, G. J., and Zhao, X.: Differences in tropical high clouds among reanalyses: origins and radiative impacts., Atmospheric Chemistry & Physics, 2020.

Yang, Q., Fu, Q., and Hu, Y.: Radiative impacts of clouds in the tropical tropopause layer, Journal of Geophysical Research: Atmospheres, 115, 2010.

Young, A. H., Bates, J. J., and Curry, J. A.: Application of cloud vertical structure from CloudSat to investigate MODIS-derived cloud properties of cirriform, anvil, and deep convective clouds, Journal of Geophysical Research: Atmospheres, 118, 4689–4699, 2013.